Master's Thesis

Experimental Studies on the Ion Separation Capabilities of LEBT Sections and High Voltage Degassing in Extraction Systems

by Daniel Born

Institut für Angewandte Physik
Johann Wolfgang Goethe-Universität

Frankfurt am Main
January 25, 2017

Assessors:
Prof. Dr. Holger Podlech
Dr. Christoph Wiesner

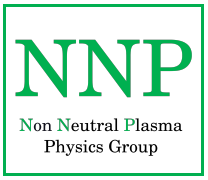

Abstract

Cleaning an ion beam from unwanted fractions is crucial for intense ion beams. This thesis will explore separation methods using a collimation channel, electric and magnetic dipoles and a velocity selector for low intensity beams on an experimental basis. In addition, statistical data of degassing events during the commissioning of a pentode extraction system for beam energies from 20 - 120 keV will be presented.

Contents

"If you always do what you've always done,
you'll always get what you've always got"
— Henry Ford

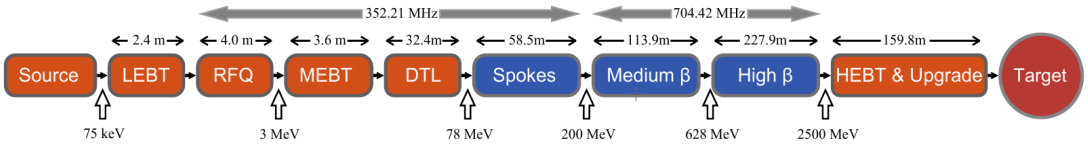

Figure 1: Layout of the European Spallation Source (ESS). Large boxes represent the ion source, beam transport sections and accelerating units. Taken from Peggs et al. [2013].

1 Introduction

1.1 Motivation

Linear accelerator designs, like the accelerator for the European Spallation Source (ESS) [Peggs et al., 2013], utilize a unitised setup (comp. Fig. 1) in order to meet the needs for high currents and beam energy as well as simplifying maintenance and development. The ion source and Low Energy Beam Transport (LEBT) section is followed by a multitude of different accelerator types, each designed for a certain energy range.

Ions can be produced from gases by impact ionisation with electrons, producing a plasma via gas discharge. The charge states depend on the energy of the electrons, their collision rate, the confinement time of the plasma as well as the type of residual gas used in the ion source. As a result, an ion source can be tuned to produce mostly one specific charge state. Correspondingly, the production rates of other charge states diminish, but do not vanish. In a plasma, different chemical compounds consisting of the available elements may appear. Thus, ion sources produce typically more than one charge state or molecular fractions (e.g. H^+, H_2^+, H_3^+ or Ar^+, Ar^{2+}) depending on the gas in the ion source. In addition, contaminating or residual gases can be ionized as well.

Unwanted ion fractions will not be transported correctly and might get lost in the following accelerator stages. Lost particles deposit energy at the position of impact according to their kinetic energy. Therefore, ensuring proper beam transportation becomes very important, especially at very high energies (comp. [Schmidt et al., 2003, 2006]). However, repetitive ion impacts with low energy at the same position can heat the beam line and damage the structure noticeably as well (comp. [Lombardi, 2014]). Therefore, unwanted ion fractions and charge states should be mostly filtered out before gaining significant energy, i.e. before leaving the LEBT.

Besides the matching of the diverging beam from the ion source into the acceptance of the first accelerator stage, there are other important tasks for a LEBT section. This might include imprinting a time structure onto a continuous beam. Correct matching of the phase space and time structure of the beam is critical in order to ensure high currents in subsequent acceleration stages.

Usually a significant amount of beam intensity is lost in the LEBT section [Dahl et al., 2002], especially if space charge effects dominate. A high current ion beam is intrinsically defocused by its space charge. This effect is most noticeable at low energies. However,

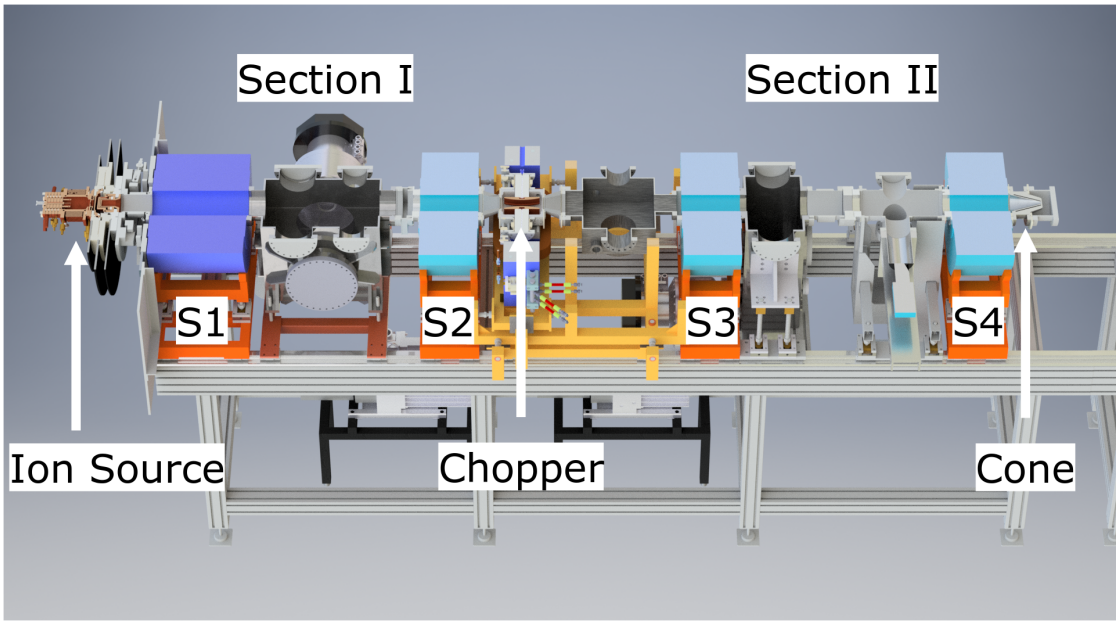

Figure 2: cross-sectional view of the FRANZ LEBT. Solenoids and the magnetic dipole of the chopper are coloured in blue. In the picture a high current ion source for neutron production is mounted. For commissioning purposes a low intensity source is used.

it can be (partly) compensated by electrons produced by impact ionisation from the residual gas. In short, a LEBT should provide beam transportation with minimal beam losses and emittance growth, which ensures beam intensity at the target. This includes the removal of unwanted ion fractions from the ion source beam and the acquisition of diagnostic data.

The LEBT section of the FRANZ (**Fra**nkfurter **N**eutronenquelle am Stern-Gerlach-**Z**entrum) accelerator is a combination of two common LEBT sections divided by a novel fast electromagnetic chopper developed and build by C. Wiesner [Wiesner, 2014]. The first section matches the beam from the ion source into the chopper. It is able to create beam pulses down to 50 ns of length [Meusel et al., 2012]. The second section matches the chopped beam into the RFQ.

Nevertheless, the question remains how the LEBT section with its lenses, the chopper and small apertures acts concerning the filtering of ions. This thesis will measure and try to separate the contributions of different filter elements. In addition, several measurements concerning the ion source, the extraction system and degassing events will be presented, which happened naturally during the commissioning process of the accelerator.

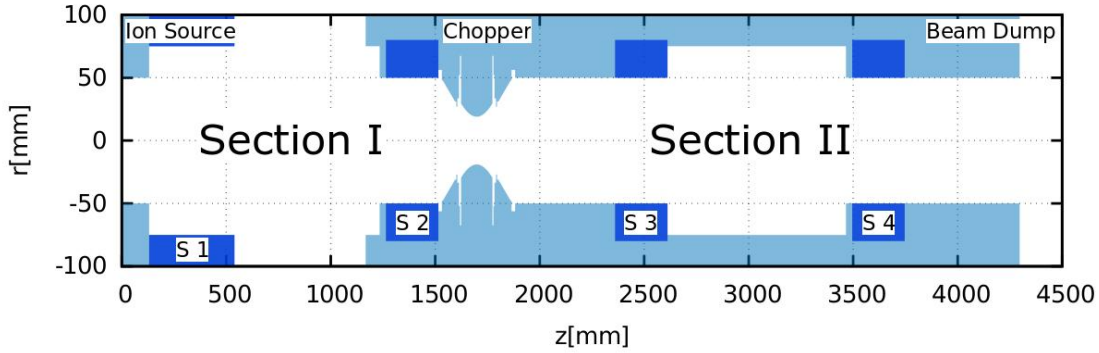

Figure 3: Schematic of the beam line according to setup 1. Solenoids are coloured in dark blue. After the pictured path the beam is stopped by a Faraday cup. The beam propagates from left to right.

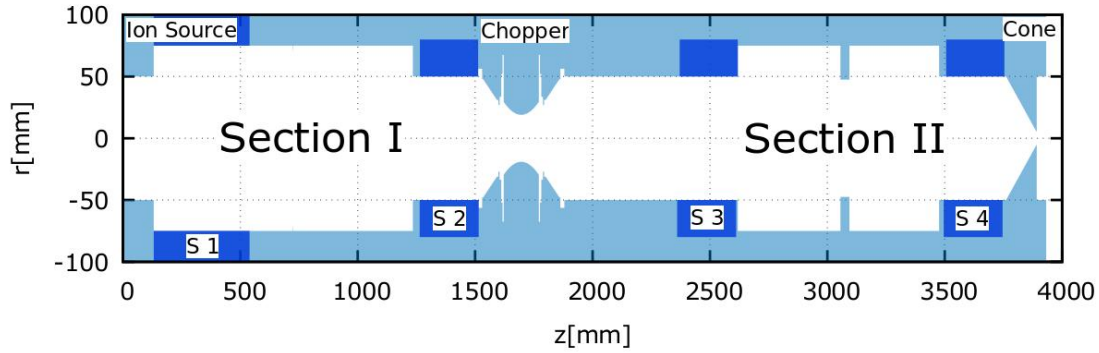

Figure 4: Schematic of the beam line according to setup 2. Solenoids are coloured in dark blue. After the pictured path the beam is stopped by an isolatedly suspended flange.

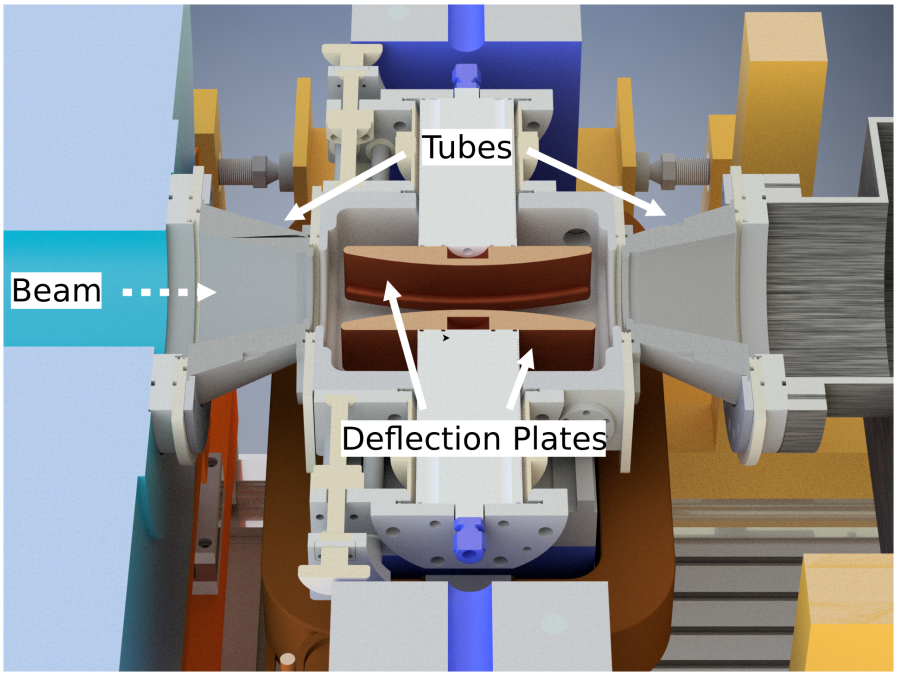

Figure 5: Half section of the electromagnetic chopper system with the isolatedly suspended tubes and deflection plates.

1.2 Experimental Setups

In Fig. 2 a CAD rendering of the LEBT according to setup 2 is shown. For all experiments, a volume type ion source which delivers about 1 mA He^+ with a pentode extraction system is installed. Two types of solenoids are used. Type I has an aperture of 100 mm, a peak on-axis field of 786 mT at 400 A and an aspect ratio of 0.4. Type II has an aperture of 150 mm, a peak on-axis field of 657 mT at 400 A and an aspect ratio of 0.37 [Lotz, 2011, p. 19]. Solenoid 1 is a type II solenoid and the other three are type I solenoids. The first diagnostic tank between the first and the second solenoid houses a moveable Faraday cup with secondary electron suppression (SES). The electromagnetic chopper is located between the second and third solenoid, followed by a preliminary cubic tank (comp. Fig. 2). Between solenoid three and four there are additional options for diagnostics, such as beam tomography [Wagner, 2013] and a current transformer. The narrowest aperture in the beam line is the 38 mm wide gap between the chopper plates (comp. Fig. 5) which breaks the rotational symmetry of the beam line. As a result of ongoing construction efforts, measurements were done with two setups of the beam line.

The first setup (comp. Fig. 3) has a 50 cm drift after the fourth solenoid and is completed via a beam dumb which inhabits a Faraday cup with SES. In the second setup (comp. Fig. 4), a cone is placed right behind solenoid 4. The beam line is finished right behind the cone via a preliminary flange. The flange and cone are electrically

isolated against the rest of the beam line. Currents created by the impact of ions can be measured, although there is no SES.

The chopper system is constructed according to setup 3 described in [Wiesner, 2014, p.49] and contains the electric and magnetic dipoles used for the filter measurements (comp. Fig. 5). Conical shortening tubes are placed up- and downstream of the dipoles. The tubes shape the distribution of the magnetic field in order to match the field of the electrostatic deflector. Tubes and deflection plates are isolated, so that the currents of impacting particles can be measured.

2 Theoretical Foundation

This brief introduction to the theoretical foundation for this thesis is based on Hinterberger [2008], Wiedemann [2007], Reiser [1994]. All calculations are non-relativistic, because particles in the LEBT section are typically not fast enough.

2.1 Charged Particle Beams

A beam consists of many individual particles propagating through an accelerator. When describing a beam, it is useful to define a moving coordinate system relative to an ideal trajectory $\mathbf{r}_0$. A particle on this trajectory is typically not affected by focusing elements, since it passes beam optics in their centre and propagates with the design velocity. A description in a fixed coordinate system is most likely to be more complicated and less intuitive. A moving coordinate system is also called Frenet-Serret coordinate system [Wiedemann, 2007, p. 22 ff]. The z-axis of the coordinate system usually points in the direction of $\mathbf{r}_0$. The x- and z-axis span a horizontal and the x- and y-axis a vertical plane with respect to the ground. The position of a given particle is calculated via:

$$\mathbf{r}(s) = \mathbf{r}_0(s) + x(s)\hat{\mathbf{x}} + y(s)\hat{\mathbf{y}} + z(s)\hat{\mathbf{z}} \tag{1}$$

with s being the position of the reference particle along the beam line and $\hat{\mathbf{x}}, \hat{\mathbf{y}}, \hat{\mathbf{z}}$ being the unit vectors for their respective axes. Particles in an accelerator have to be electrically charged to be accelerated. Beam manipulation is done by electromagnetic forces.

$$\mathbf{F} = q(\mathbf{E} + \mathbf{v} \times \mathbf{B}) \tag{2}$$

With the electric field $\mathbf{E}$, the magnetic induction $\mathbf{B}$, the charge q of the ion and the particle velocity $\mathbf{v}$. The effects of the magnetic and electric fields on the particles are discussed in detail in section 2.2. A simple way to characterize an ion beam is by its beam current. It is defined similar to an electric current:

$$I_{\text{beam}} = \int \mathbf{j} \mathrm{d}\mathbf{A} = \int q n_{\text{i}} \mathbf{v}_{\text{i}} \mathbf{dA} \tag{3}$$

$\mathbf{j}$ is the ion current density, $\mathbf{v_i}$ the ion velocity, n_{i} the ion density, $\mathbf{A}$ the considered oriented area and q the charge of an ion. By taking into account that the area is defined by the expansion of the beam, and assuming that the beam density is homogeneous, the equation simplifies to:

$$I_{\text{beam}} = q n_{\text{i}} v_{\text{i}} A_{beam} \tag{4}$$

In accelerator experiments, it is often useful to have a high beam current, leading to more events which can be analysed. The weak law of large numbers states that the probability for a deviation of the mean from the expectation value of independently identically distributed (iid.) random variables approaches to zero when the number of iid. random variables approaches to infinity (comp. [Bosch, 2011, p. 151]). Each measurement of a system in a certain configuration can be interpreted as an iid. random

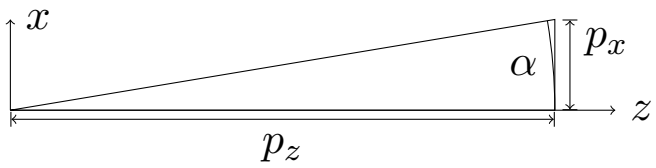

Figure 6: Schematic that shows that the opposite legs length is equal to α in radians for small α.

variable. Therefore, the weak law of large numbers states that multiple measurements of the same configuration reduce the probability that the average of the measured values does not match the physical value with respect to probabilistic errors. This statistical effect does not affect the systematic errors of the measurements.

Phase Space

The phase space is a different approach to describing a beam. In general, the state of one particle is fully described by its six coordinates (i.e. x, y, z, p_x, p_y, p_z) in phase space. A whole beam with N particles is therefore characterized by a point in this $6N$ dimensional space. Its time evolution is represented by a trajectory in phase space. However, with the use of some assumptions it is possible to consider only a subspace that is still meaningful.

Instead of treating the beam as an ensemble of interacting particles, the particles are treated individually without interactions. As a result, the phase space can be reduced from $6N$ dimensions to six. Liouville's theorem states that the phase space density of the ensemble in the six dimensional space stays constant if it evolves via a Hamiltonian ([Reiser, 1994, p.64]). Particle interaction can be reintroduced via effective or average fields.

In order to speak of a beam, the momenta p_x, p_y perpendicular to the direction of propagation z should be small. Therefore, almost their entire momentum is facing in the direction of the beam $p_z \approx p$. As a result, a paraxial approximation can be done. It is used to replace the perpendicular momenta p_y, p_y as the respective angle x', y' between the particle trajectory and the design trajectory via Taylor expansion of $\tan(\alpha) \approx \alpha$.

$$\frac{p_x}{p_z} = \tan(\alpha) \approx \alpha \tag{5}$$

$$\rightarrow x' = \alpha \approx \frac{p_x}{p_z} \tag{6}$$

A schematic of this approximation is shown in Fig. 6. For practical purposes, the particles are characterized via the angle α rather than their transversal momentum $p_{x,y}$. From all particles in a beam, the maximum angle x'_m is called divergence and the maximum distance x_m from the design beam axis is called width of the beam. In order to understand the time evolution of the particles in particle phase space, it is helpful to take a look at two-dimensional projections of this space.

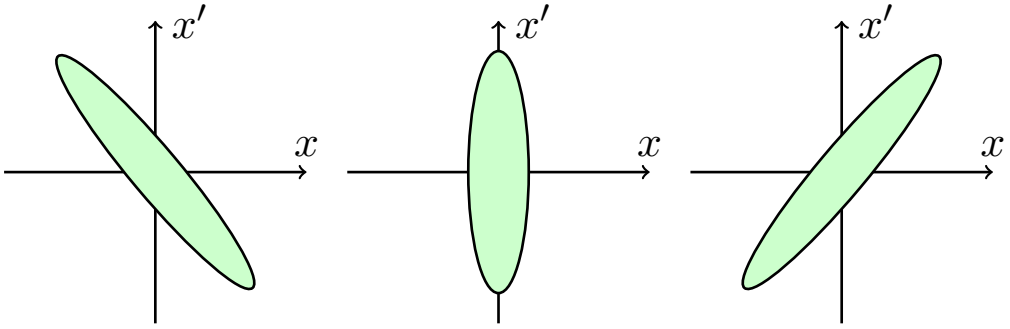

(a) convergent beam (b) focus (c) divergent beam

Figure 7: The elliptic envelopes of an example beam in trace space are shown. During a simple drift (from (a) to (b) to (c)) the ellipses will be sheared in the direction of x which maintains their area.

Emittance

The emittance is one of the key measures used in accelerator physics when trying to quantify the quality of a beam. In the following, two ways to define the emittance of a beam are covered [Reiser, 1994, p.57 ff].

The more intuitive approach is to consider the area that the particles cover in a certain particle phase space projection (i.e. xx' or yy'). The spaces which these planes represent are called trace spaces [Reiser, 1994, p. 57]. All definitions and calculations that will be derived for the xx' space are valid in the yy' space as well. Trace space schematics of a typical convergent beam (a), a focus (b) and a divergent beam (c) are shown in Fig. 7. The emittance ϵ_x is defined as the area that is covered by all beam particles in the corresponding trace space xx' divided by π. Only if the area is a vertical or horizontal ellipse, the emittance is the product of the divergence and the width of the beam:

$$\epsilon_x = \frac{A_{xx'}}{\pi} = x_{m\perp} x'_{m\perp} \tag{7}$$

Emittance is usually measured in mm mrad. Calculating the emittance via the covered area only considers the area of the points in trace space but does not account for the the distribution of this area. The shape and continuity of the area might be significantly altered by non-linear effects. Such a case is illustrated in Fig. 8. The difference in this case is extreme and artificial, but segmentation or emergence of several arms apart from the typical elliptical shape are a quite common phenomenon. An example is the RFQ input distribution of a beam simulation for the MYRRHA accelerator [Zhang et al., 2012]) shown in Fig. 8 (c). Alternatively, the rms emittance can be defined via the statistical moments of the beam. In general, the n^{th} moment about c is defined as follows [Sachs and Hedderich, 2008, p. 209ff][Reiser, 1994, p. 358]:

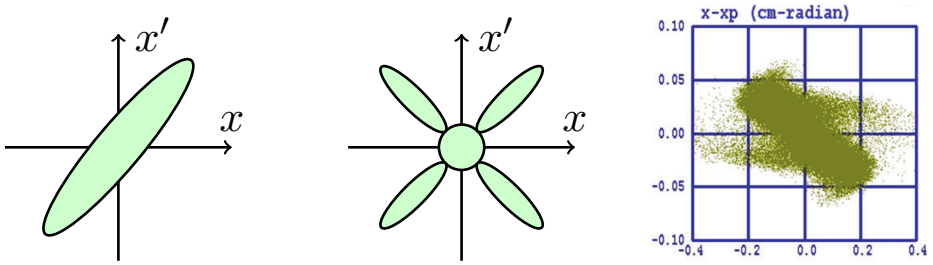

(a) (b) (c)

Figure 8: (a) and (b) show an exaggerated illustration of the shortcoming of the emittance definition according to Eq. (7). The sizes of the green areas are identical. (c) shows a simulation of a input distribution for the MYRRHA RFQ. Taken from Zhang et al. [2012].

$$\overline{x_i^n} = \int_{-\infty}^{\infty} (x_i - c)^n f(x_1, x_2, ...) \mathrm{d}x_1 \mathrm{d}x_2 ... \tag{8}$$

With c being the reference point of the moment and $f(x)$ the distribution function of x. The moments are called central moments, if the reference c is the expectation value μ of the distribution. The second central moment of $\bar{x_i}$ is its variance. In case the reference point of the moment is not specified, the offset c is considered to be zero. Therefore, the first moment (c = 0) is equal to the expectation value of the distribution. A definition of the rms emittance is possible via centred moments, because they do not depend on the choice of origin for the coordinates. The rms emittance $\tilde{\epsilon}_x$ is defined as:

$$\tilde{\epsilon}_x = \sqrt{\overline{x^2}\ \overline{x'^2} - \overline{xx'}^2} \tag{9}$$

The factor $\overline{xx'}^2$ indicates that the beam is either diverging or converging [Reiser, 1994, p.58]. In case the phase space distribution has an axial symmetry to the x- or x'-axis, the term $\overline{xx'}^2$ vanishes, because it considers the sign of x and x'. This is the case for the focus shown in Fig. 7 (b), which can be created by the drift of a converging beam. Past its focal point, a drifting beam becomes divergent. The definition of the rms emittance via statistical moments does account for the distribution of the area in phase space. The ratio of the emittance divided by the rms emittance is an indication how populated the tail of a distribution is [Reiser, 1994, p. 360]. However, assuming that the particles do not interact directly with each other and the fields can be expressed in terms of scalar or vector potentials, the volume and density of the particles in 6d - phase space remain constant. This circumstance is called Liouville's Theorem [Reiser, 1994, p.62ff]. If the projections $(xx', yy'zz')$ do not couple with each other via forces, the area of the projections in Fig. 7 remains constant as well. Hence, it is sufficient to consider only a tilted ellipse which surrounds all particles of the beam in a phase space projection [Wiedemann, 2007, p. 158]:

$$\hat{\gamma}x^2 + 2\hat{\alpha}xx' + \hat{\beta}x'^2 = \epsilon_x \tag{10}$$

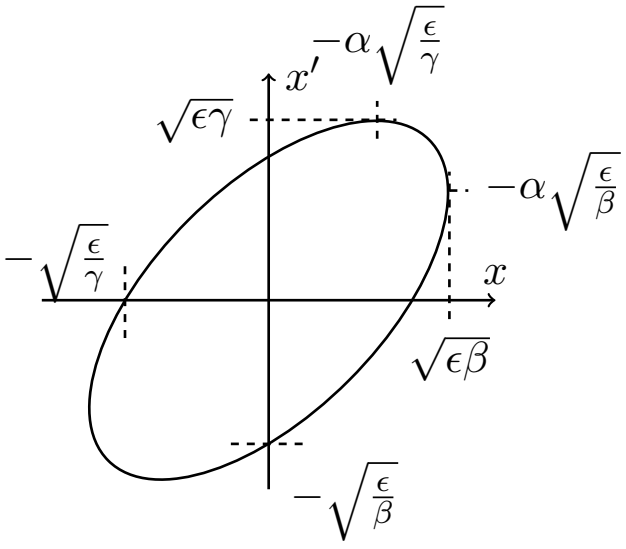

Figure 9: Elliptic phase space area with the corresponding Twiss parameters. Redrawn according to [Wiedemann, 2007, p. 158].

The parameters α, β and γ are called Twiss Parameters. α is a measure for the amount of tilting. For $\alpha = 0$ the ellipse has a vertical position. β indicates how much the ellipse is spread in x direction and γ measures the same for the x' direction. Fig. 9 shows the geometrical meaning of the Twiss parameters.

In order to characterise a beam, it is not sufficient to specify the emittance in x and y. In addition, the total current of the ions is an important figure, too. For accelerator units which use particle pulses, the distribution of the particles in z is of interest, too. It is possible to define an equivalent of the trace spaces for z, which plots the spread in z against the energy deviation of the particles.

Brightness

The emittance of a given beam can be highly improved by using slits and apertures to cut off particles with large offsets. As a result the emittance decreases, but the beam current decreases as well. Therefore, the brilliance, defined as the density of current per trace space area, is introduced[Reiser, 1994, p.61] to take the ion current into account as well. The brightness may vary across the area of beam.

$$B = \frac{\mathrm{d}I}{\mathrm{d}S\mathrm{d}\Omega} \tag{11}$$

With $\mathrm{d}\Omega$ being the solid angle in trace space and $\mathrm{d}S$ the solid angle in spacial space. For general usage the average brightness of a beam is calculated, which is more comparable to the emittances of a beam.

$$\bar{B} = \frac{I}{V_4} \tag{12}$$

With V_4 being the Volume of the trace spaces $V_4 = \iint \mathrm{d}S\mathrm{d}\Omega$. For a distribution with uniform elliptic trace space projections, the brightness can be calculated from the emittances.

$$\bar{B} = \frac{2I}{\pi^2 \epsilon_x \epsilon_y} \tag{13}$$

2.2 Separation Methods

2.2.1 Collimator

Collimation will be used to limit the beam spatially at certain points. This restriction will influence the whole phase space if applied repeatedly [Pfister et al., 2011]. The most simple way of doing so is to put slits and small apertures in the path of the beam. Particles with a big offset or divergence are removed. As a result, the beam emittance can be improved by reducing beam intensity at the outer regions of the phase space ellipse.

Following this argument, every beam line is an implicit collimator due to its physical properties. Once an ion hits anything inside the accelerator, it is considered to be lost. If it collides with a metallic surface, it might lose a significant amount of energy, is most likely to be neutralized by the electrons provided by the metal and might be reflected from the surface. As a result, it can no longer be transported by the electromagnetic optics.

In case of the FRANZ LEBT the collimation is achieved with solenoids in combination with the given apertures of the beam line. As a result, the cleaning of the beam which might happen due to the collimation is a result of the beam matching process. Under the assumption of an ideal box shaped magnetic field, the focal length of a particle beam passing a solenoid can be calculated analytically (comp. [Pozimski, 1990, p.17]):

$$f = \frac{1}{k \sin(kL)} \qquad \Big| \quad k = \frac{qB}{2mv} \tag{14}$$

With the refractive power k, the magnetic induction B, the length of the solenoid L and the charge q, velocity v and mass m of the particle. For a given solenoid, the focal length only depends on the refractive power, which itself depends on the particle charge and momentum as well as the magnetic induction. Therefore, a solenoid acts as a filter for the particle momentum as well as its charge state. In case of equally charged particles, it acts as a momentum filter only.

Another implication of this result is that, for high intensity ion beams, an adjustment of the refraction power to the current beam momentum is necessary, which is connected to the beam energy. This is especially true if the beam energy is supposed to be varied during a measurement. Otherwise, beam losses might cause damage during these processes. A possible solution for this task will be presented in section 3.

The design energy for protons in the FRANZ LEBT is 120 keV [Schweizer et al., 2014]. For commissioning purposes, helium ions are used because they only appear in one molecular fraction and are simpler to handle. Because helium has about four times the mass of a proton, they have the same momentum as protons with a fourth of the

proton's velocity. As a result, the needed energy can be calculated accordingly:

$$p_1 \stackrel{!}{=} p_2 \tag{15}$$

$$\eta \cdot m_1 = m_2 \tag{16}$$

$$\rightarrow E_{\mathrm{kin2}} = \frac{p_2^2}{2m_2} = \frac{p_1^2}{2\eta m_1} = \frac{E_{\mathrm{kin1}}}{\eta} \tag{17}$$

With the index marking the two separate ion species. Hence, the helium ions need an energy of 30 keV to match momentum with the design protons. When handling ion beams with high intensity, which are planned for the future of FRANZ, space charge effects caused by the electrostatic repulsion of the ions become relevant. A measure for the strength of these effects is the generalized perveance K [Reiser, 1994, p.197]. The following equation assumes a non-relativistic ion beam with no space charge compensation.

$$K = \frac{I}{U_{\mathrm{acc}}^{\frac{3}{2}}} \left(\frac{1}{4\pi\epsilon_0 \sqrt{(\frac{2q}{m})}} \right) \tag{18}$$

With the acceleration voltage U_{acc}, the ion charge q, the ion mass m and the vacuum permittivity ϵ_0. In order to create a He^+ beam with equal space charge forces and momentum compared to a 120 keV H^+ beam with 1 mA of current, a 30 keV He^+ beam with only 63 μA of beam current is needed. Accordingly, 200 mA of H^+ at 120 keV are equivalent to 12.5 mA He^+ at 30 keV. The 1 mA He^+ test beam at 40 - 50 keV used for the measurements in this thesis is chosen to be above the space charge force and momentum of 2 mA H^+ at 120 keV, which is the nominal current and energy for the fist operation phase of FRANZ [Schmidt, 2015, p. 16][Wiesner et al., 2015, p. 13]. The calculated values only represent the perfect matched cases. With the help of the theorem of intersecting lines, the necessary width for an energy window to accept a perfect beam can be calculated. The following calculation uses the variables given in Fig. 10. The equation below is a direct result from the theorem of intersecting lines for an under-focused beam shown in Fig. 10 (a):

$$\frac{r_p}{r_A} = \frac{f + \Delta f_+}{\Delta f_+} \tag{19}$$

$$\rightarrow \frac{\Delta f_+}{f} = \frac{1}{\frac{r_p}{r_A} - 1} \tag{20}$$

In analogy, the result can be derived for an over-focused beam shown in Fig. 10 (b):

$$\frac{\Delta f_-}{f} = \frac{1}{\frac{r_p}{r_A} + 1} \tag{21}$$

It is worth mentioning that the possible deviation Δf from the nominal focus point is entirely determined by the geometry of the beam line. In order to translate the maximum deviation of the focus from the nominal focal length into a window of possible energies

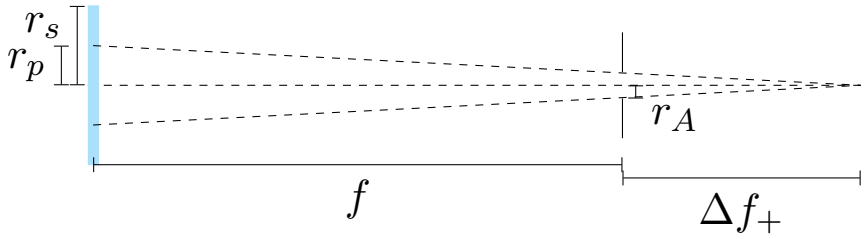

(a) under-focusing of beam

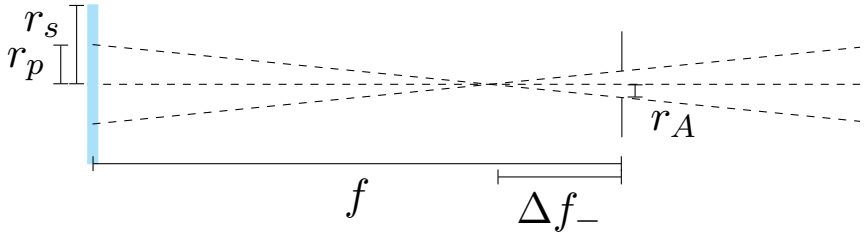

(b) over-focusing of beam

Figure 10: Schematic of possible offset of beam focus, which would still be completely transported. A solenoid is shown in blue. (a) shows the case for under-focusing (b) shows the case for over-focusing r_s is the inner radius of the solenoid, r_A the radius of the aperture and r_p the distance of the particle to the z-axis which is considered.

or momenta of the particles, Eq. (14) is used. It is important to generally note that a calculated energy windows is specific to the particle species, because in this case the filtering depends on the particles' mass as well. Small values of k are assumed to obtain an analytical result.

$$f = \frac{1}{k^2 L} \quad \Big| \; k = \frac{qB}{2p} \tag{22}$$

$$\rightarrow p = \frac{qB}{2}\sqrt{fL} \tag{23}$$

$$\rightarrow E_{\text{kin}} = \frac{p^2}{2m} = \frac{(qB)^2}{8m} fL \tag{24}$$

However, this simplification should not be used for *absolute* estimations on the FRANZ LEBT, because the deviations in the focal length $\frac{\Delta f}{f}$ might be small compared to error introduced by the assumption of a small k. Nevertheless, it can be used to estimate an analytical result for the *relative* width of momentum and energy accepted by the geometry. It follows from eq. (20), (21) and (23).

$$\frac{\Delta p_\pm}{p} = \pm\left(\sqrt{1 \pm \frac{\Delta f_\pm}{f}} - 1\right) \tag{25}$$

$$\frac{\Delta E_\pm}{E} = \frac{\Delta f_\pm}{f} \tag{26}$$

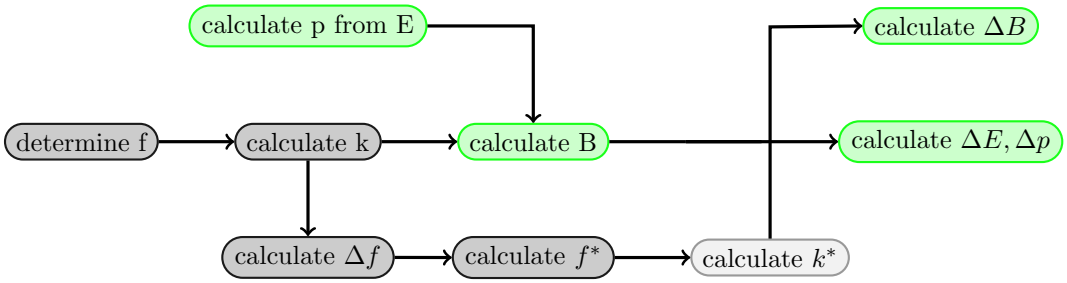

Figure 11: Flow chart displaying the process of calculating different acceptance windows for the collimation filter. Calculations coloured in grey only depend on the geometry of the beam line. A star indicates that the variable includes the focal length deviation Δf. Optional steps are in light grey.

In case of the energy, a compact expression for the estimation of the asymmetry caused by the difference in the upper and lower bound can be derived:

$$\frac{\Delta E_\pm - \Delta E_\mp}{\Delta E_\pm} = \frac{\frac{\Delta f_\pm}{f} - \frac{\Delta f_\mp}{f}}{\frac{\Delta f_\pm}{f}} = \frac{\Delta f_\pm - \Delta f_\mp}{\Delta f_\pm} = 1 - \frac{r_p \mp r_A}{r_p \pm r_A} \tag{27}$$

This calculation shows that given the simplification $\sin(kL) \approx kL$, the accepted region above the desired energy is always larger than the region below. Alternatively, k can be obtained by numerical methods, such as Newton's method. The simplified eq. (23) and (24) become:

$$p = \frac{qB}{2k} \tag{28}$$

$$E_{\text{kin}} = \frac{1}{8m}\left(\frac{qB}{k}\right)^2 \tag{29}$$

The logic behind the calculation for the filter width of the collimation is displayed in Fig. 11. The focal length and the energy of the particles are the parameters that are determined by the geometry and the user. They are needed in order to calculate the refractive power which determines the necessary magnetic field of the solenoid. With the help of eq. (20) and (21) the offset of the focal length is calculated. The new focal lengths are converted into the desired quantities (B, E or p) with either the simplified Eq. (23) or with a detour via Newton's method and Eq. (29). The offset is obtained by subtraction from the original value. Note that all other quantities are assumed to be accurate. In the calculations, solenoid type II is assumed to have an effective length of 324 mm (comp. [Lotz, 2011, p.30]) and the distance of the particle from the z-axis r_p is assumed to be half the radius of the solenoid. In Tab. 1 estimations on the energy width for the LEBT of FRANZ according to setup 2 are shown. H^+ ions with an energy of 120 keV are supposed to be transported by design. The other values are calculated in order to compare them to measurements during the commissioning process. Protons

f [mm]	k [$\frac{1}{m}$]	r_p [mm]	r_A [mm]	Δf_+ [mm]	Δf_- [mm]
3557	0.83826	37.5	5	547	418

(a) fixed parameters and results of the estimations

species	E[keV]	B[mT]	ΔE_+[keV]	ΔE_- [keV]	$\frac{\Delta E_+}{E}$	$\frac{\Delta E_+ + \Delta E_-}{E}$
H^+	120	83.9	18.8	14.3	15.7 %	27.6 %
He^+	30	83.9	4.7	3.6	15.7 %	27.6 %
He^+	40	96.9	6.3	4.8	15.8 %	27.6 %
He^+	50	121.3	7.8	6.0	15.6 %	27.6 %

(b) variable parameters and results of the energy estimations

Table 1: Estimations of the filter effect caused by collimation with respect to energy. Table (a) presents the parameters and results which do not depend on the energy or species of the ions. They are determined by the geometry. Table (b) shows the assumed parameters and the results. ΔE_+ and ΔE_- are the energy deviations allowed above (+) and below (-) of the design energy.

species	E [keV]	p [$\frac{\text{MeV}}{\text{c}}$]	B [mT]	Δp_+ [$\frac{\text{MeV}}{\text{c}}$]	Δp_- [$\frac{\text{MeV}}{\text{c}}$]	$\frac{\Delta p_+}{p}$	$\frac{\Delta p_+ + \Delta p_-}{p}$
H^+	120±5	15± 0.4	83.9	1.1	0.9	7.5 %	13.7 %
H_2^+	120±5	21.2 ±0.5	-	-	-	-	-
H_3^+	120	26	-	-	-	-	-
He^+	30	15	83.9	1.2	0.9	7.5 %	13.7 %
He^+	40	17.3	96.9	1.3	1.1	7.5 %	13.7 %
He^+	50	19.4	108.3	1.5	1.2	7.5 %	13.7 %

Table 2: Estimations of the filter effect caused by collimation with respect to momentum. Energy and momentum of the different hydrogen ions are given as a reference point. Calculations are based on the values given in Tab. 1 (a)

must have four times the kinetic energy of helium in order to produce equal results, which is consistent with the factor between momentum and kinetic energy derived in Eq. (17). The relative impact of the filter should be independent of the energy or momentum for small k (comp. Eq. (27)), which approximately fits the calculation.

A solenoid is usually considered to be a momentum-sensitive filter. In Eq. (14), the ratio of the particle charge and the momentum are the only particle property defining the focal point. The consideration of other quantities than momentum introduces more dependencies. In case of the energy, the mass of the particles additionally influences the focal point (comp. Eq. (29)). As a result, a valid energy window is restricted to particles with a specific mass as well. Therefore, the estimations of Tab. 1 are repeated for the particle momentum in Tab. 2. The total relative filter width of the collimation filter is about 13 % of the reference momentum. Based on this estimation, it is expected that, at 120 keV beam energy, almost no hydrogen ions except H^+ are able to pass the LEBT section. But this is only true for the particles that pass the solenoid at half of

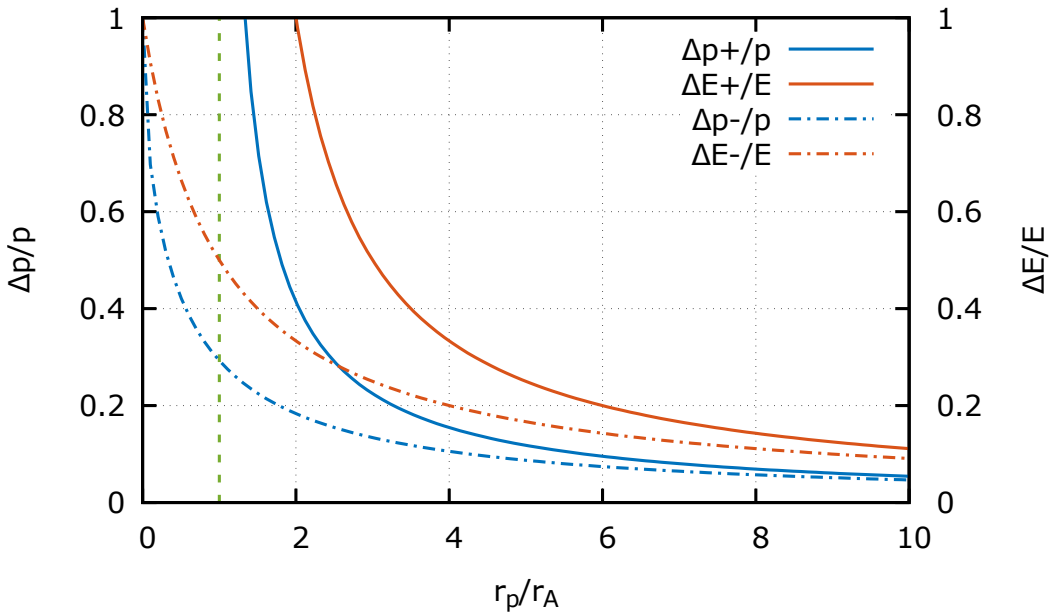

Figure 12: The relative filter strength, i.e the accepted deviations from momentum and energy in percent is shown according to eq. (25) and (26), with respect to the ratio of radial distance of the particle to the z-axis and the aperture radius.

its inner radius. The distance of the particle to the z-axis r_p has a major effect on the calculations. Fig. 12 shows the dependence of the relative filter effect on the ratio between the distance of the particle to the z-axis and the radius of the aperture. The equations are derived using eq. (25) and (26) in combination with eq. (20) and (21):

$$\frac{\Delta p_{\pm}}{p} = \pm\left(\sqrt{1 \pm \frac{1}{\frac{r_P}{r_A} \mp 1}} - 1\right) \tag{30}$$

$$\frac{\Delta E_{\pm}}{E} = \frac{1}{\frac{r_P}{r_A} \mp 1} \tag{31}$$

The filter effect decreases rapidly if the radius of the aperture approaches the radial distance of the particle to the z-axis (comp. Fig. 12, green dashed line). The filter effect is very different for above- and below-reference deviations, especially for small ratios. If the ratio between the distance of the particle to the z-axis and the radius of the aperture is one, the accepted momentum width for smaller-than-reference values maintains to be 25 % of the reference value, whereas particles with a larger-than-reference momentum are not limited. The limits for r_p approaching r_A while $r_p \geq r_A$ are calculated in order

to emphasise the asymmetry in filter strength (comp. Fig. 10).

$$\lim_{r_p^+ \to r_A} \Delta f_+ = \infty \tag{32}$$

$$\lim_{r_p^+ \to r_A} \Delta f_- = \frac{f}{2} \tag{33}$$

$$\lim_{r_p^+ \to 0} \Delta f_- = f \tag{34}$$

These limits show that the accepted offset of the focal point increases indefinitely for deviations above the focal length reference, but has a limit for deviation below the focal length reference. However, in the limit of the particle being on the axis, the filter effect vanishes.

To sum up, collimation by solenoids highly affects particles in the outer areas of the beam. Halo particles of any kind that do not match the specified charge momentum ratio are very likely to be filtered. This effect declines rapidly if the distance of the particles to the z-axis is about three times the radius of aperture they are supposed to pass. However, particles with smaller-than-reference momentum are more rigorously filtered in the small radius regime than particles with larger-than-reference momentum. For small k the ratio $\frac{r_A}{r_P}$ scales inversely with the relative filter width.

As a result, after passing the LEBT section of FRANZ in its recent state (setup 2), the beam should have no significant halo particles from other fractions, due to the small apertures the beam has to be transported through.

2.2.2 Electric Dipole

The deflection of a single particle by an electric dipole can be estimated by an homogeneous electric field. Boundary field effects will be neglected in this approximation. The particle starts at the origin with its design velocity **v**. The homogeneous electric field begins in the origin and extends for a defined length s_1. The orientation and polarity of the electrical field is chosen such that positive particles are deflected in the direction of **x**. The force created by an electric field is given by:

$$F_{El} = qE \tag{35}$$

With E being the electrical field strength and q being the charge of the particle. The resulting constant acceleration is:

$$a = \frac{qE}{m} \tag{36}$$

With m being the mass of the particle. The deflection is assumed to take place in the xz-plane. In terms of kinetic energy the resulting equations of motion are:

$$t = \frac{s_{z1}}{v} = \frac{s_{z1}}{\sqrt{\frac{2qU_{\text{acc}}}{m}}} \tag{37}$$

$$s_x = s_{x0} + v_{x0}\frac{s_{z1}}{\sqrt{\frac{2qU_{\text{acc}}}{m}}} + \frac{E}{4U_{\text{acc}}}s_{z1}^2 \tag{38}$$

$$v_x = v_{x0} + \sqrt{\frac{q}{2mU_{acc}}}Es_{z1} \tag{39}$$

With s_{x0} and v_{x0} being the initial offset from the design trajectory and velocity in the direction of x and s_{z1} being the length of the deflection area in the direction of z. In case of an additional drift of length s_{z2} in z after the deflection, the position in x becomes:

$$s_x = s_{x0} + \underbrace{\frac{v_{x0}}{\sqrt{\frac{2qU_{\text{acc}}}{m}}}(s_{z1} + s_{z2})}_{\text{drift by initial velocity}} + \underbrace{\frac{E}{4U_{\text{acc}}}s_{z1}^2}_{\text{drift by deflection in dipole}} + \underbrace{\frac{Es_{z1}s_{z2}}{2U_{\text{acc}}}}_{\text{drift after dipole}} \tag{40}$$

By assuming that the ion has no initial offset or velocity in x the equation simplifies to:

$$s_x = \frac{E}{4U_{\text{acc}}}s_{z1}^2 + \frac{Es_{z1}s_{z2}}{2U_{\text{acc}}} \tag{41}$$

The offset by the deflection is proportional to the electric field and anti-proportional to the original acceleration voltage. The angle of deflection is defined by:

$$\tan(\alpha) = \frac{v_x}{v_z} = \frac{s_1 E}{2U_{\text{acc}}} \tag{42}$$

This simple approximation can be made more useful using effective quantities [Wiesner, 2014, p.12]. The idea is to describe an electric field with fluctuations along the axis $\mathbf{E}(z)$

by a homogeneous field E_{x0}. For deflection purposes, one field component should be prominent, i.e. $E_x \gg E_y, E_z$. Hence, only contributions in this direction are accounted. The method of effective fields neglects the dependence of the particle trajectory on the actual spacial distribution of the electrical field. The length of an homogeneous field with strength E_0 is calculated via:

$$l_{\mathrm{eff}} = \frac{1}{E_0} \int E_x(z) \mathrm{d}z \tag{43}$$

However, the electrical dipole alone will not be used in the FRANZ facility as a static stand alone deflector, because the LEBT section does not include bends. It is used to keep certain particles in a straight line as part of the Wien filter configuration.

2.2.3 Magnetic Dipole

The deflection of a single particle by a magnetic dipole can be approximated by a homogeneous magnetic field. Fringe field effects will be neglected. The Lorentz force always acts perpendicular to the propagation direction:

$$\mathbf{F}_{\mathrm{Mag}} = q(\mathbf{v} \times \mathbf{B}) \tag{44}$$

With $\mathbf{B}$ being the magnetic induction. Therefore, the Lorentz force acts as a centripetal force. For the purpose of filtering particles, the magnetic field is aligned perpendicular to the velocity, since the norm of the vector product is proportional to the sine of the included angle. The equivalence of the magnetic and centripetal force yields:

$$r_{\mathrm{L}} = \frac{m|\mathbf{v}|}{|q|B} \tag{45}$$

r_{L} is called Larmor radius. The amount of deflection can be calculated via the Larmor radius and the equation for an arc of a circle.

$$x_D = r_{\mathrm{L}} - \sqrt{r_{\mathrm{L}}^2 - z^2} \tag{46}$$

For obvious reasons, this equation is only valid for $0 < z < r_{\mathrm{L}}$. For $z > r_{\mathrm{L}}$ the particle would most likely be reflected by the dipole. Like in section 2.2.2, the effective field method can be used to transform complex field shapes into homogeneous ones. The effective field length can be calculated in analogy.

$$l_{\mathrm{eff}} = \frac{1}{B_0} \int B_y(z) \mathrm{d}z \tag{47}$$

2.2.4 Wien Filter (Velocity Selector)

A Wien filter consists of a homogeneous electric and magnetic field. The correct perpendicular alignment of both fields and the particle beam causes opposing forces to act on the charged particles passing the filter. In the event that the electric and magnetic forces cancel each other, the particles remain unaffected by the fields. The condition which follows for the fields is called Wien condition.

$$F_B = F_E \tag{48}$$
$$qvB = qE \tag{49}$$
$$v = \frac{E}{B} \tag{50}$$

With the velocity v and the charge q. B and E represent the magnetic and electric fields and F_B and F_E their respective forces. By assuming that the ion beam has been extracted and accelerated by a given electric field, the Wien condition can be expressed in terms of the (effective) acceleration voltage U_{acc} and the charge-mass ratio of the particles $\frac{q}{m}$.

$$v = \sqrt{\frac{2qU_{\text{acc}}}{m}} \tag{51}$$
$$\rightarrow \frac{q}{m} = \frac{E^2}{2U_{\text{acc}}B^2} \tag{52}$$

Therefore, the Wien filter, originally a velocity selector (comp. Eq. (50)), can be used to select the ions which have been accelerated via an electric field according to their charge-mass ratio. Given that two ions with different masses have the same energy, their corresponding difference in velocity is calculated as follows:

$$E_{\text{kin1}} \stackrel{!}{=} E_{\text{kin2}} \tag{53}$$
$$\eta \cdot m_1 = m_2 \tag{54}$$
$$\rightarrow v_2 = \sqrt{\frac{2E_{\text{kin2}}}{m_2}} = \sqrt{\frac{2E_{\text{kin1}}}{\eta m_1}} = \frac{v_1}{\sqrt{\eta}} \tag{55}$$

In case an ion does not match the Wien condition, it is deflected according to:

$$F_{\text{def}} = qE - qvB \tag{56}$$
$$= q\left(E - \sqrt{\frac{2qU_{\text{acc}}}{m}}B\right) \tag{57}$$

The factor ζ denotes how much a non-matching ion deviates from the charge-mass ratio the Wien filter is designed for.

$$\zeta\left(\frac{q}{m}\right)_{\text{design}} = \left(\frac{q}{m}\right)_{\text{ion}} \tag{58}$$

However, this method can also be used to calculate the effect of deviations in the kinetic energy.

$$\zeta \left(qU_{\mathrm{acc}}\right)_{\mathrm{design}} = \left(qU_{\mathrm{acc}}\right)_{\mathrm{ion}} \tag{59}$$

The usage of the same factor ζ is intentional, because it has the same effect. Therefore, it can either be considered to be the offset factor for the charge-mass ratio while assuming constant kinetic energy or vice versa. With eq. (52) and (58) the deflecting force simplifies to:

$$F_{\mathrm{def}} = qE\left(1 - \sqrt{\zeta}\right) \tag{60}$$

If positive particles have a smaller charge-mass ratio than the design ratio of the filter, the force of the magnetic field is weaker and they are deflected in the direction of the electric field (positive deflection force). The decrease in magnetic force during the deflection is neglected, because only small deflection angles are assumed. Thus, the total deflection can be approximated by simple classical mechanics. Without loss of generality, the deflection is assumed to take place in the xz-plane.

$$t = \frac{s_{z1}}{v} = \frac{s_{z1}}{\sqrt{\frac{2qU_{\mathrm{acc}}}{m}}} \tag{61}$$

$$s_x = s_{x0} + v_{x0}\frac{s_{z1}}{\sqrt{\frac{2qU_{\mathrm{acc}}}{m}}} + \frac{E}{4U_{acc}}(1 - \sqrt{\zeta})s_{z1}^2 \tag{62}$$

$$v_x = v_{x0} + \sqrt{\frac{q}{2mU_{acc}}}Es_{z1}(1 - \sqrt{\zeta}) \tag{63}$$

With s_{x0} and v_{x0} being the initial offset from the design trajectory and velocity in the direction of x and s_{z1} being the length of the deflection area in the direction of z. In case of an additional drift of length s_{z2} in z after the deflection, the position in x becomes:

$$s_x = s_{x0} + \underbrace{\frac{v_{x0}}{\sqrt{\frac{2qU_{\mathrm{acc}}}{m}}}(s_{z1} + s_{z2})}_{\text{drift by initial velocity}} + \underbrace{\frac{E}{4U_{\mathrm{acc}}}(1 - \sqrt{\zeta})s_{z1}^2}_{\text{drift by deflection during filter}} + \underbrace{\frac{Es_{z1}s_{z2}}{2U_{\mathrm{acc}}}(1 - \sqrt{\zeta})}_{\text{drift after filter}} \tag{64}$$

By assuming that the ion has no initial offset or velocity in x, the equation simplifies to:

$$s_x = \frac{E}{4U_{\mathrm{acc}}}(1 - \sqrt{\zeta})s_{z1}^2 + \frac{Es_{z1}s_{z2}}{2U_{\mathrm{acc}}}(1 - \sqrt{\zeta}) \tag{65}$$

For calculation purposes, the electrical and magnetic field are assumed to be applied over a length of 138 mm. The electric field is assumed to be $235.5\,\mathrm{kV\,m^{-1}}$. The drift after the deflection is supposed to be 1.8585 m, which is equivalent to the distance from the chopper plates until the beginning of solenoid 4. Fig. 13 visualizes the offset created by the mismatch of filter properties. With respect to filtering ions by charge, the corresponding deviation factors of H^+, H_2^+, H_3^+ are $1; 0.5; 0.33$. As a result, the filter effect on the different ion fractions should be noticeable, because a offset of about 60 mm

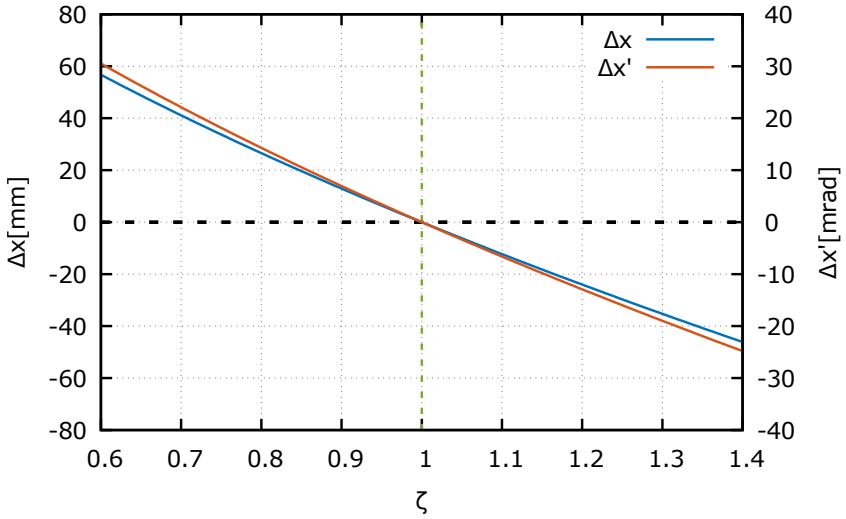

Figure 13: Visualisation of the offset in the deflection plane created by the Wien filter. The offset distance and momentum are shown in dependence on the deviation factor ζ.

is larger than the inner radius of the solenoid 4 (50 mm). The combination of offsetting the unwanted ion fractions from the beam axis and removing them afterwards efficiently by collimation is expected to yield a solid filtering result. With respect to energy, the filter effect is more subtle but still significant. An energy offset of 10 % leads to a particle offset of about 10 mm, which will prevent the particles from passing through the cone in front of the RFQ.

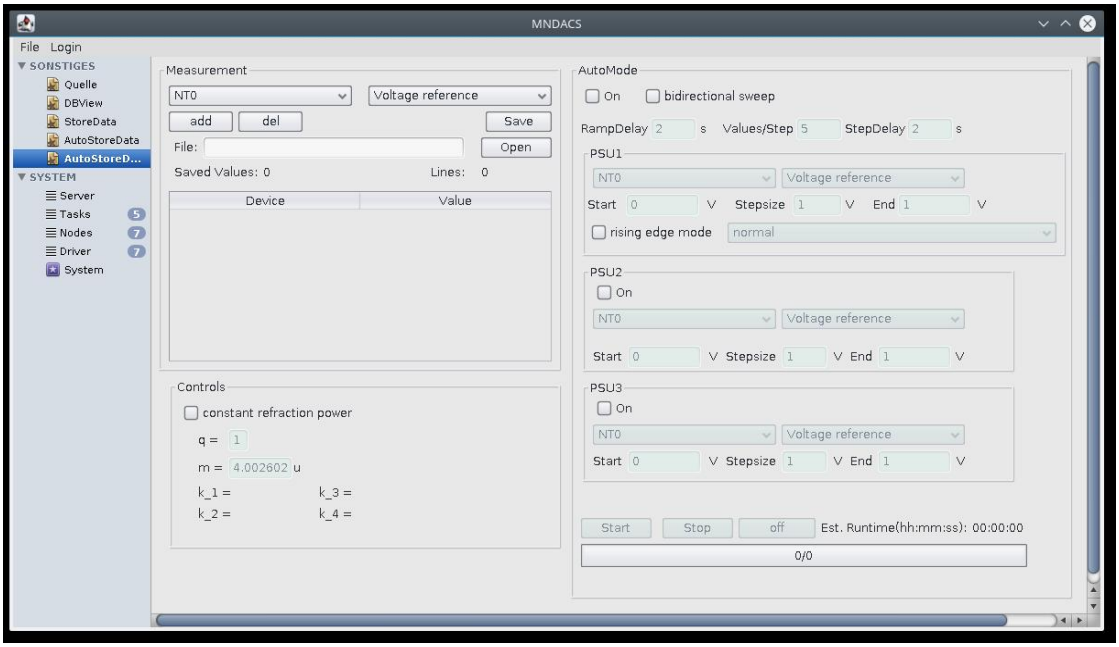

Figure 14: Recent design of the measurement script GUI. It is divided into measurement, control and auto-mode sections.

3 Experimental Preparations

Before actual measurements concerning the ion separation capabilities of the LEBT can be conducted, a stable and undisturbed operation of the accelerator elements has to be ensured. This includes the development of automated (measurement) script with the goal of improving the comfort for experimentalists, as well as increasing the accuracy and amount of collected data. This is especially important for data acquisition which is sensitive with respect to time.

3.1 Development of Measurement Script

The FRANZ accelerator is controlled by the MNDACS control system developed by C. Wagner[1], which is written in Java. Extensions, such as the aforementioned measurement script, can be implemented in the MNDACS environment. Once all installations at the FRANZ facility are completed, all power supplies and beam diagnosis concerning the FRANZ facility are supposed to be controllable or at least readable with the use of the control system. This central system enables almost synchronous data collection from all diagnostic elements with high repetition rates.

The graphical user interface (GUI) is shown in Fig. 14. The design evolved over time as more functionality was needed. In the measurement section, the power supplies and

[1] https://sourceforge.net/projects/mndacs/ (13.06.2016)

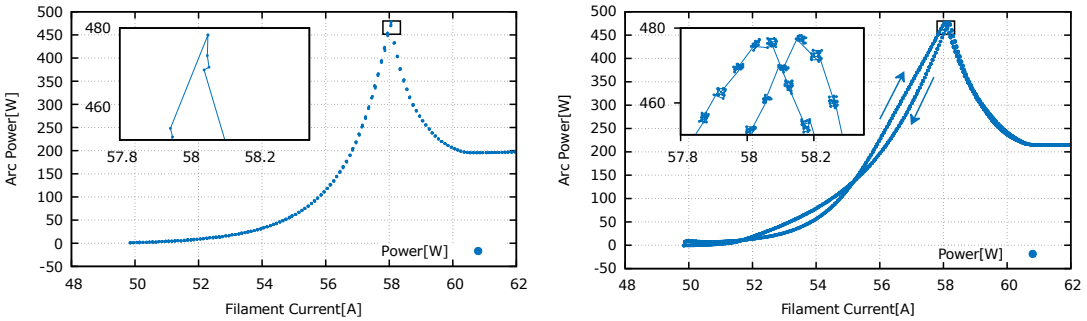

(a) Manual measurement

(b) Automated measurement

Figure 15: Comparison of a manual measurement (a) and an automated measurement (b) with MNDACS. Data points are connected according to their time of measurement. The magnified section shows the improved smoothness and distribution of the data points.

diagnostic read-only channels are selected which will be recorded. The control section enables the script to perform automatic corrections to certain beam parameters during the actual measurement. In the auto mode section, up to 3 power supplies are selected to be controlled simultaneously. A ramping routine is defined via a start value x_0, step size dx and end value x_f. Additionally, power supplies are able to return to their initial value via the bidirectional option.

In the long run an autopilot routine, comparable to auto pilots in air planes or prototype cars, is supposed to control the parameters of the ion source and the LEBT section with the help of simulation code and live data provided by the diagnostics. In this way, the necessary stability and usability can be achieved during the actual operation time for the affiliated experiments without having to concentrate extensively on the accelerator operation.

The acquisition of the data is controlled via three values. A delay t_d can be defined which prevents the system from collecting data after a power supply step to wait for the experiment to reach equilibrium. The duration of a measurement run is usually dominated by the number of values n_v the script should collect per power supply step and the pause time t_p between the collection of two values. The total time is calculated via:

$$t_{\text{tot}} = \underbrace{\frac{x_f - x_0}{dx}}_{\#\text{ of steps}} \underbrace{(t_d + n_v * t_p)}_{\text{Duration per step}} \tag{66}$$

Due to limitations given by the response times of the power supplies and the network, a pause time t_p of at least two seconds is recommended. Otherwise, latency issues with the data acquisition system start to occur.

Fig. 15 shows a comparison between a manual and an automatic measurement of a plasma ignition process in a volume type ion source. The script is configured to take a seven second long thermalisation break plus 20 measurements every step. The pause between measurements is two seconds. The automatic measurement shows an improved

smoothness in the magnified area in addition to small distributions or clusters of the points belonging to one current step. As a result, the stochastic error of the data can easily be estimated.

Furthermore, the shape of these distributions is an indication of how close the system is to equilibrium during the measurements. The more the system deviates from equilibrium, the harder it becomes to identify the individual clusters which belong to a certain step. In an extreme non-equilibrium state, it will not be possible to assign the data points to a certain measurement step, because their distributions are completely blurred. Last but not least, with the help of the bidirectional option it is possible to observe a subtle hysteresis effect.

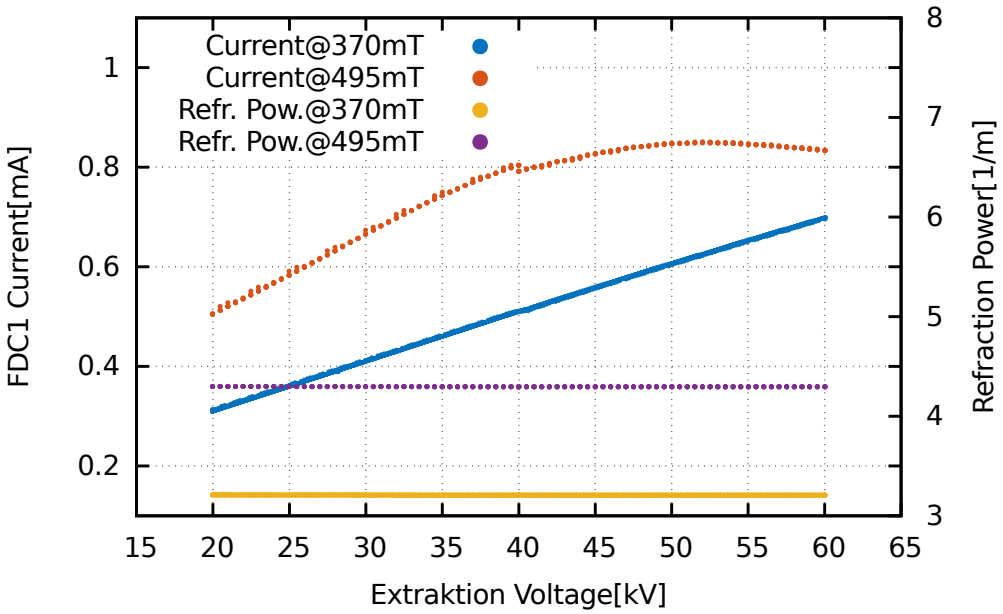

Figure 16: The blue and red points show the current in FDC1 right behind the first solenoid. The yellow and purple points represent the corresponding refraction power. The reference point for the magnetic field is 40 kV.

3.2 Constant Refraction Power – an Auto Operator Example

The magnetic field of a solenoid acts on charged particles like an optical lens on light. The refraction power of a solenoid is, in analogy to optics, a measure which indicates how much a certain ion species is deflected. In linear approximation it is given by [Hinterberger, 2008, p. 144ff]:

$$k = \frac{qB}{2mv} = \frac{B}{2}\sqrt{\frac{q}{2mU_{\mathrm{acc}}}} \tag{67}$$

With B being the magnetic induction, m the mass, v the velocity and q the charge of the ions and U_{acc} the (effective) acceleration voltage . Hence, the effect of the solenoid on faster or heavier ions is weaker.

The FRANZ accelerator is designed to transport up to 200 mA of current at 120 keV [Schweizer et al., 2014]. In the LEBT sections, such a beam has a power of up to 24 kW. If the energy of the beam is altered, the refraction power has to be adjusted in a way that it stays constant for most of the ions. Otherwise, beam losses and energy deposition will occur, which might cause damages. Solving Eq. (67) for the magnetic induction B gives:

$$B = 2k\sqrt{\frac{2mU_{\mathrm{acc}}}{q}} = \frac{2k}{q}\sqrt{2mE_{\mathrm{kin}}} \tag{68}$$

This equation can be used to keep the solenoids at a constant refraction power with respect to the beam energy. Fig. 16 shows a measurement with a low intensity He^+ beam, validating its proper functionality. The refraction power is calculated by using Eq. (67) and the measured extraction voltage. The reference point of the magnetic fields is at an extraction voltage of 40 kV. From this starting point, a measurement with increasing and one with decreasing voltage was done. The slight offset in the current at 496 mT and 40 kV is caused by this circumstance.

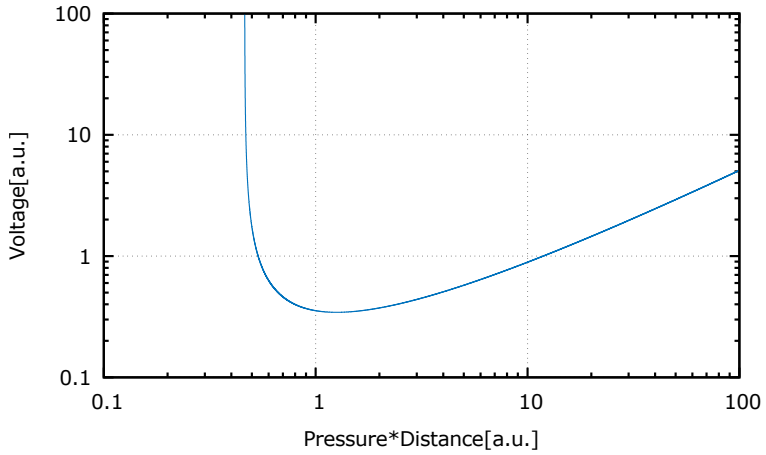

Figure 17: Typical example of a Paschen curve.

3.3 Conditioning of Extraction System

The conditioning of the extraction system for high voltages is a mandatory task. The working hypothesis is that impurities on the surfaces are reduced in the process of applying increasing voltages. Impurities are particles or microscopic edges on a material's surface. An eventual voltage breakdown with arc discharge will most likely occur in the position of an impurity, where the electrical field is amplified. Repeated low power arc discharges are supposed to clean the surface in a way that it will support increasingly high voltages. During an arc discharge, the desorption process is supposed to increase the pressure.

In theory, the maximum applicable voltage to the extraction system without a flashover is determined by Paschen's law. It determines the maximum voltage between perfectly planar electrodes as a function of their distance d and the pressure p. Fig. 17 shows a typical Paschen curve, which is specific for each gas. A measurement from Marić et al. [2014] shows that, for helium gas, the left slope is at about 1 mbar cm. As a result, arc discharges begin to occur at a pressure of about 1 mbar in an extraction system with a 1 cm gap. It is worth noticing that their measurement suggest that above 10 kV the discharge threshold is only weakly dependent on the actual applied voltage.

In volume type ion sources, there is typically a high pressure gradient in the extraction system. In our case, the pressure decreases from $2 \cdot 10^{-2}$ mbar in the plasma chamber to about $1 \cdot 10^{-7}$ mbar in the first diagnostic tank. As a result, there is a molecular gas flow from the ion source in the direction of the extraction system [Umrath et al., 1997, p.15].

If the ion source is switched off and the gas inlet is closed, the pressure in the ion source reduces to $4.5 \cdot 10^{-4}$ mbar or lower. Hence, for conditioning purposes, the sensitivity of the extraction system to arc discharges should be decreased by turning off the ion source and closing the gas inlet. In addition, the power supplies powering the ion source seem to be less sensitive to damages by discharges when switched off. Whether

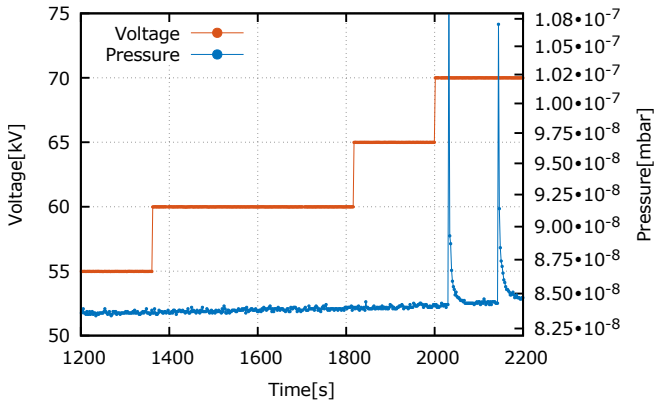

(a) 5000 V steps

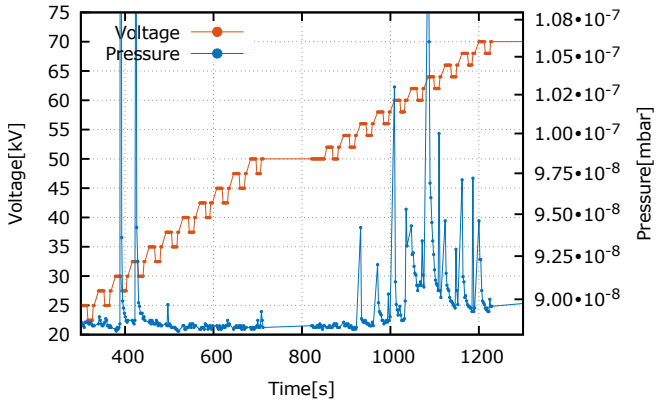

(b) 2500 V + 2000 V pattern

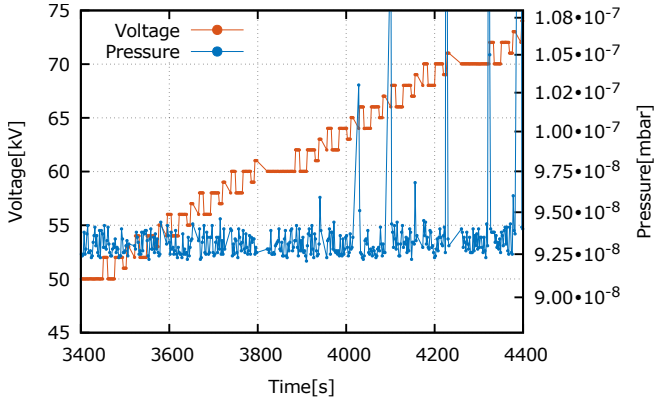

(c) 2000 V pattern

Figure 18: Comparison of different conditioning methods. Measurement (a) took place two days before (b) and (c) which are taken from the same session. The time range and maximal pressure is identical in all plots. Minimal pressure is scaled to show the pressure baseline.

or not a shut-down ion source diminishes the efficiency of the conditioning process is yet undetermined. In general, the possibility of gas inclusions opening on the surface and producing a statistical increase in pressure exists. During the gas release, the Paschen limit might be exceeded, which will cause a voltage breakdown. Over time, the gas inclusions will open statistically, but during maintenance, which can require a breaking of the vacuum, new inclusions will be created due to the inevitable ventilation of some beam line sections. Hence, a good conditioning procedure should prepare the surface with respect to impurities and gas inclusions. In addition, an automated and efficient conditioning procedure can reduce downtimes to a minimum.

Fig. 18 shows excerpts from different conditioning sessions. The most simple way of conditioning consists of increasing the voltage stepwise until degassing events happen (comp. Fig. 18 (a)). Then the voltage is slightly decreased until the pressure stabilizes. The procedure is repeated until the desired voltage is reached without degassings. If this process is done manually, it turned out to be very time consuming. In fig. 18 (b) and (c) the voltage is controlled by the script described in section 3.1, which increases the voltage in patterns with different steps. The graphs suggest that the frequency and intensity of degassing events might depend on the method with which the voltage is changed over time. Using the script turned out to be significantly less time consuming.

During the conditioning process up to 120 kV, 34.5 h of data with a time resolution of 2 s was collected with the script. In Fig. 19, the number of degassing counts in dependence on an upper and lower voltage threshold are shown. A pressure increase is considered to be a degassing if, during the 2 s time resolution, the increase exceeds a threshold Δp. A priori, this threshold is set to $\Delta p = 1 \cdot 10^{-8}$ mbar in order to find thresholds for a minimum and maximum limit in voltage change. A lower limit is supposed to cut of noise from the power supply read out. The upper limit should filter voltage breakdowns with arc discharges. The red dotted lines mark the chosen values. According to Fig. 19 (b) most of the degassings which coincide with a drop in voltage are total voltage breakdowns.

Fig. 20 shows the attempt to find a pressure threshold. In this histogram, degassings are counted in a bin size of $1 \cdot 10^{-9}$ mbar around the pressure increase Δp. But besides the general decline of noise and increasing uncertainties due to the limited sample size at higher Δp, there is a yet unexplained spike just below $1 \cdot 10^{-8}$ mbar. However, it is not possible to define a simple threshold for the variation in pressure. The dependence of the data on the choice of binning is shown in Fig. 21. The blue graph shows bins which are equally sized throughout the magnitudes. The yellow one uses one hundred bins for each magnitude, which is equal to increasing the bin size by a factor of 10 per magnitude. The stepwise increment of the bins affects the number of total counts, but has no substantial influence on the shape. The stairway-like behaviour below $1 \cdot 10^{-9}$ mbar indicates that, at this magnitude, the resolution of the measurement device is a limiting factor. Above $6.5 \cdot 10^{-8}$ mbar, the method of scaled bins inflates the number of counts artificially, whereas the equally sized bins become very small and only contain 0 or 1 counts. Furthermore, the total amount of counts per bin drops below 15 in the scaled case. As a result, all values above $6.5 \cdot 10^{-8}$ mbar are neglected.

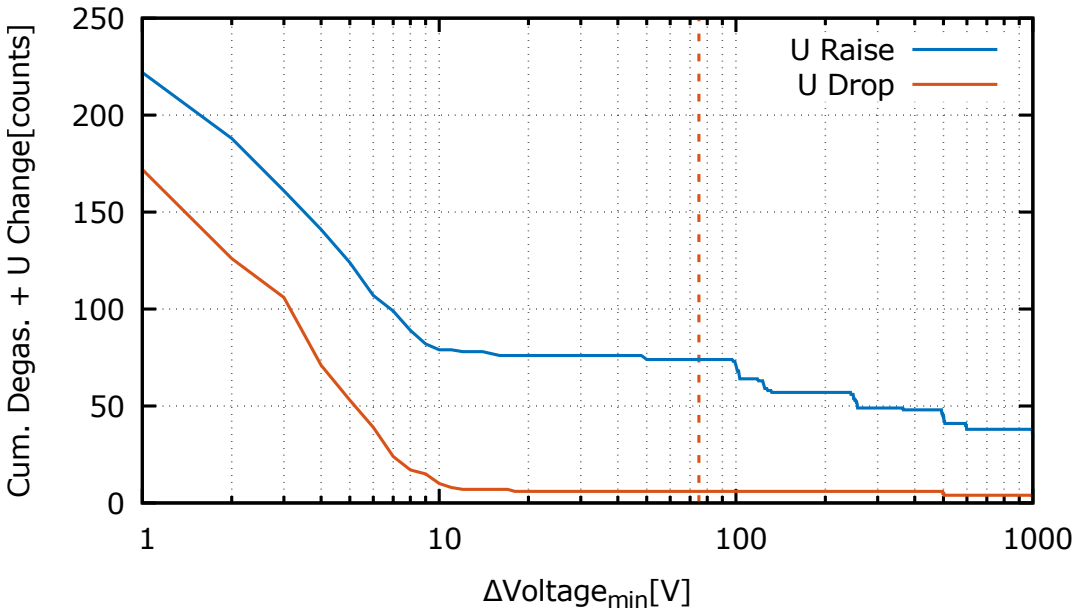

(a) Minimum ΔVoltage threshold

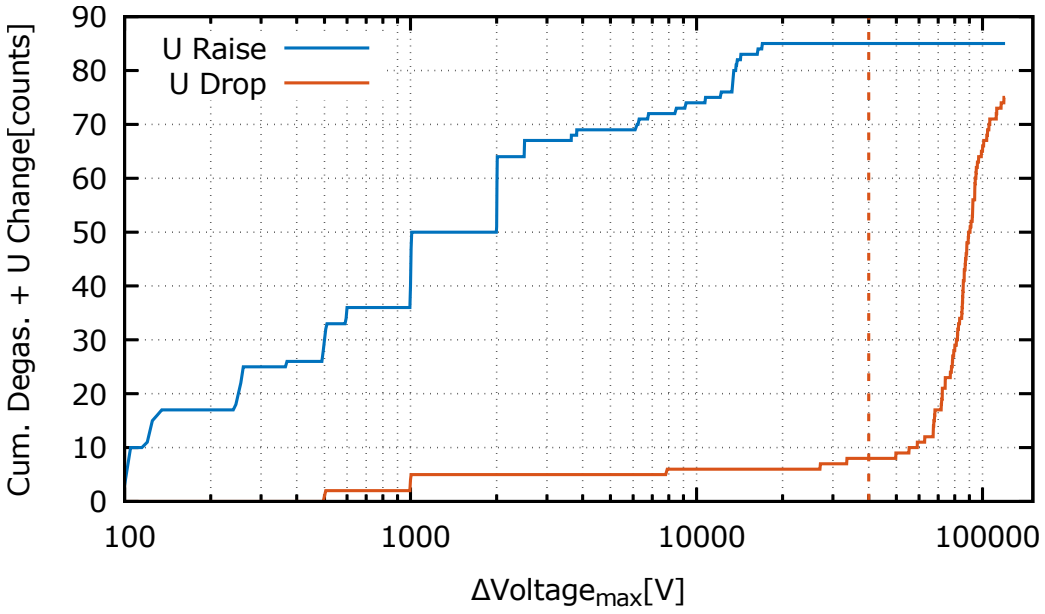

(b) Maximum ΔVoltage threshold

Figure 19: Both graphs show the number of degassing events in dependence of the minimum and maximum thresholds. The dashed red lines show the value which was chosen for further analysis.

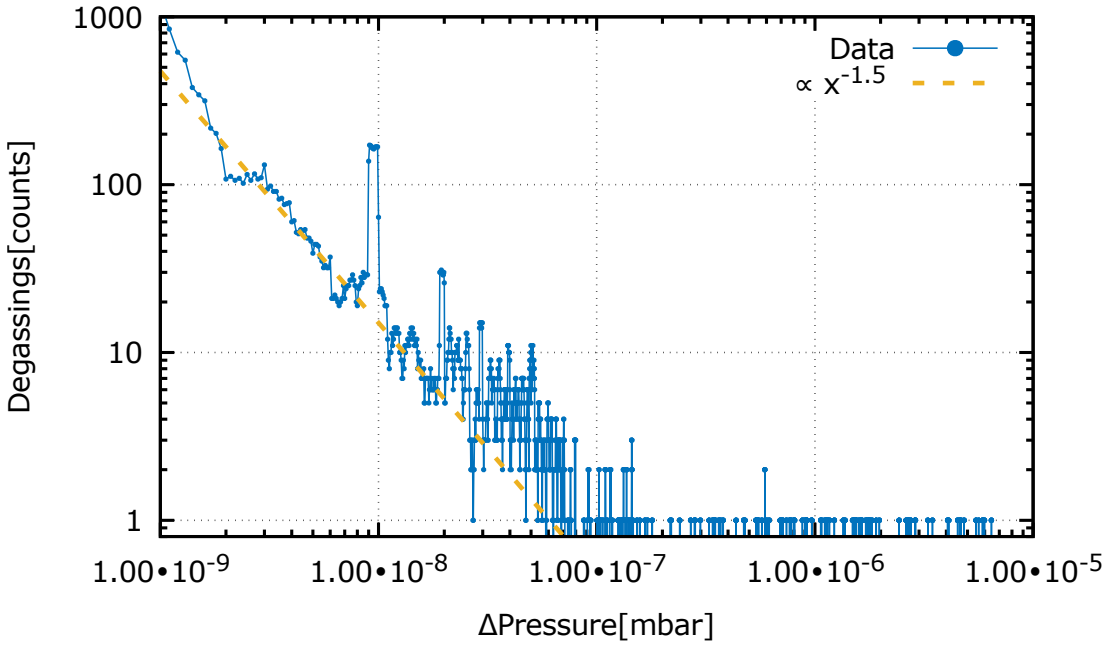

Figure 20: The number of degassings is plotted against the rise in pressure in a histogram. The bin size is $1 \cdot 10^{-9}$ mbar.

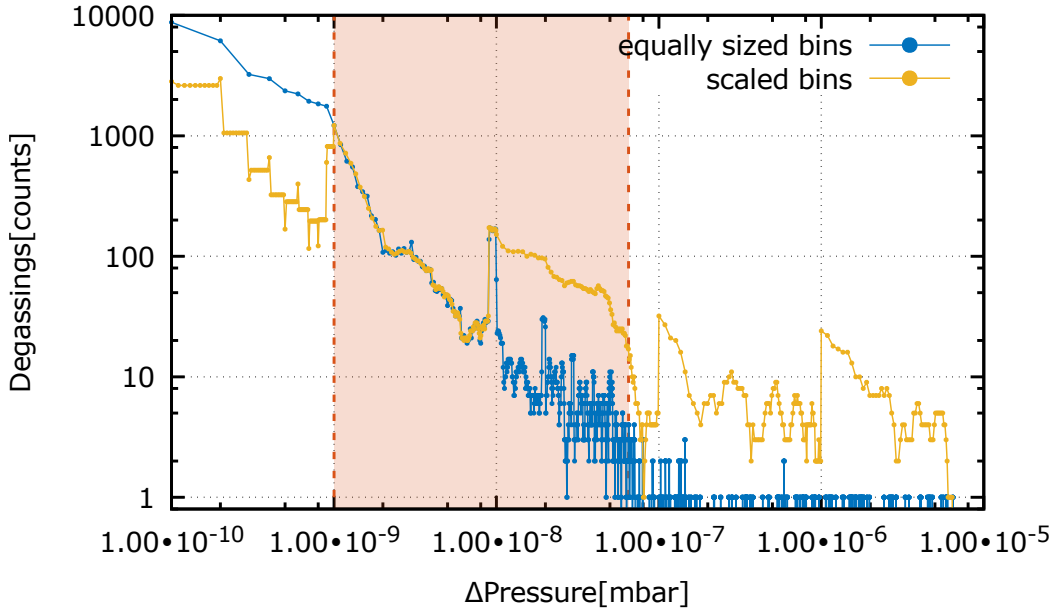

Figure 21: Comparison between equally spaced and per magnitude increasing bin sizes. Values in the pale red area should neither be affected by the resolution of the measurement device nor limited by the sample size.

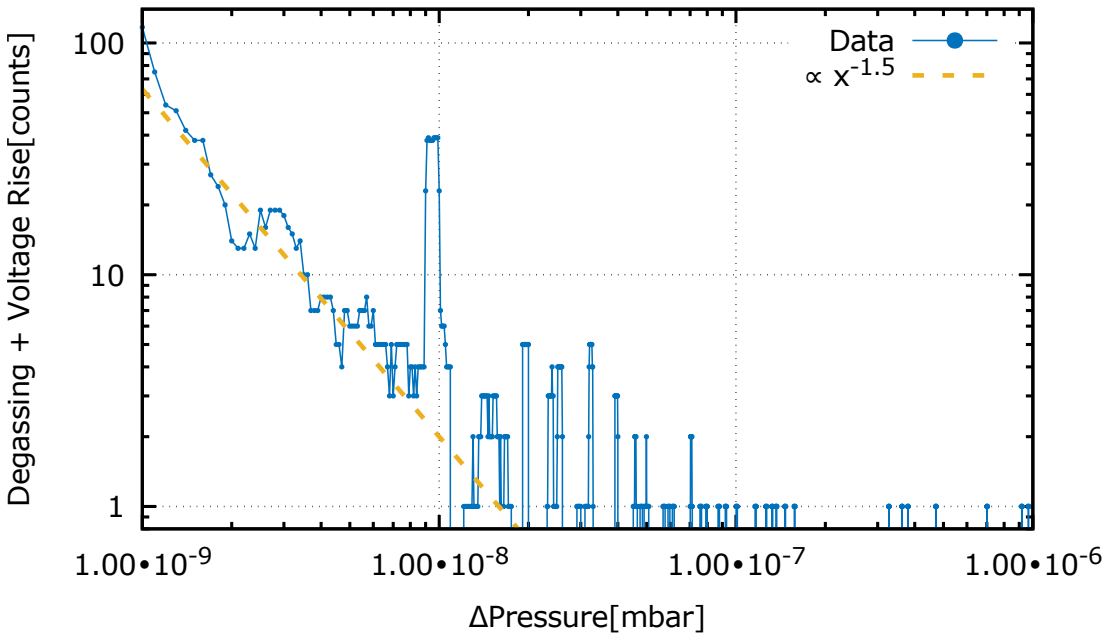

(a) Simultaneous voltage rise and degassing

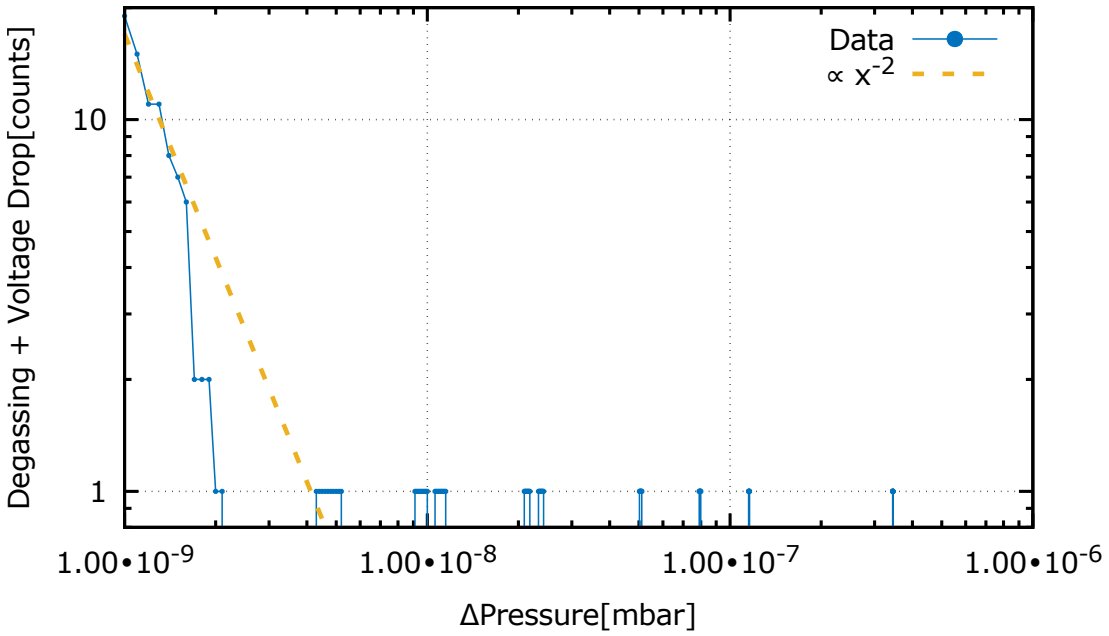

(b) Simultaneous voltage drop and degassing

Figure 22: In analogy to Fig. 20, the data is plotted in a histogram like fashion with a bin size of $1 \cdot 10^{-9}$ mbar. Only degassing events which happen simultaneously with a voltage change are counted.

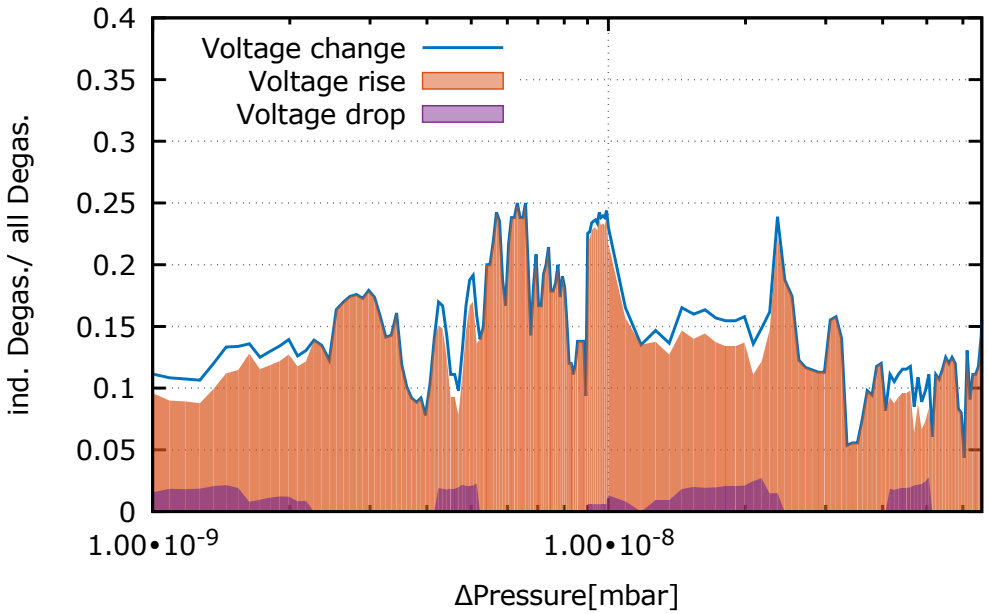

Figure 23: The relation between the number of induced and total degassings are plotted against the pressure change.

In a next step, only degassing events are counted, which happen simultaneously with a controlled change in voltage. The relation between probabilistic and "induced" degassings is supposed to indicate if the degassing events can be induced by voltage changes or not. Fig. 22, in analogy to power spectral density plots, shows the rises and drops in voltage. Note that the ratio of voltage rises to dips in the used data is about 6:5. The plot will be compared to the reference plot with all degassings (see Fig. 20). In the case of a voltage increase, the general shape is similar to the reference plot. The number of counts decreases equally fast and the spike just below $1 \cdot 10^{-8}$ mbar is present as well. In contrast, the voltage drop cases occur very rarely and their incidence declines rapidly around $2 \cdot 10^{-9}$ mbar. In Fig. 23, the relation between induced and all degassings is shown in dependence of the pressure change. Voltage drops only have a one percent effect on the total number of degassings. In contrast, voltage rises contribute to up to 25 % of degassings. On average, their effect is at least in the ten percent range.

As a preliminary result, there are indications that increasing the voltage in steps between 125 V to 3000 V can induce degassings that do not need to produce voltage breakdowns. The degassing frequency can be increased by 10 % to 25 %.

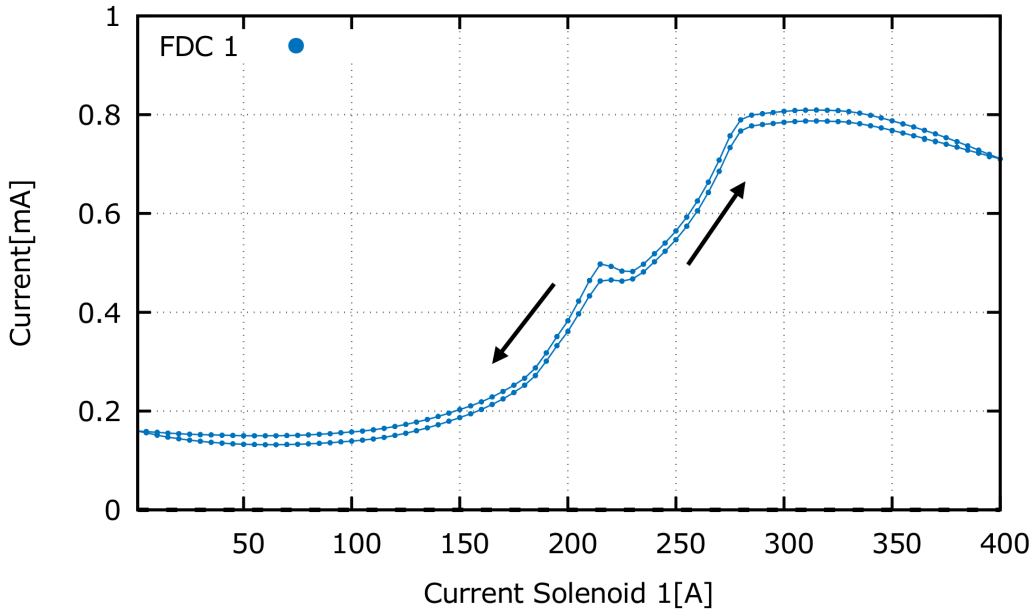

Figure 24: Current of He^+ beam at 50 keV measured after solenoid 1.

4 Measurements on Filter Capabilities

For a systematic investigation of the filter effects in the LEBT section, the influence of beam matching via the solenoids is investigated first. In addition, the effects of a dipole on a matched beam are investigated.

4.1 Solenoids

4.1.1 Variation in Focusing Strength

A beam energy of 50 keV for He^+ is chosen for the solenoid measurements. This energy is 20 keV above the energy, which corresponds to an equal momentum of H^+ (comp. Eq. (17)) as a worst-case scenario. These measurements validate, supplement and complement low energy measurements (1.6 mA He^+ at 14 keV) and simulations done by T.F. Nowottnick who investigated the solenoid channel [Nowottnick, 2014]. The following observations are consistent with the low energy measurements and reveal even more details due to their enhanced resolution.

The transmission through solenoid 1, measured by the Faraday cup in the diagnostic tank of section I, is shown in Fig. 24. The current is expected to rise smoothly until it reaches an optimum which should be followed by a descending current. However, the initial transmission decreases for currents below 100 A which corresponds to 165 mT. Possible explanations for this effect are an influence by the small magnetic field on the electrons in the plasma sheath of the extraction hole, which might alter the shape of the plasma meniscus. Another explanation is a decompensation of the ion beam by

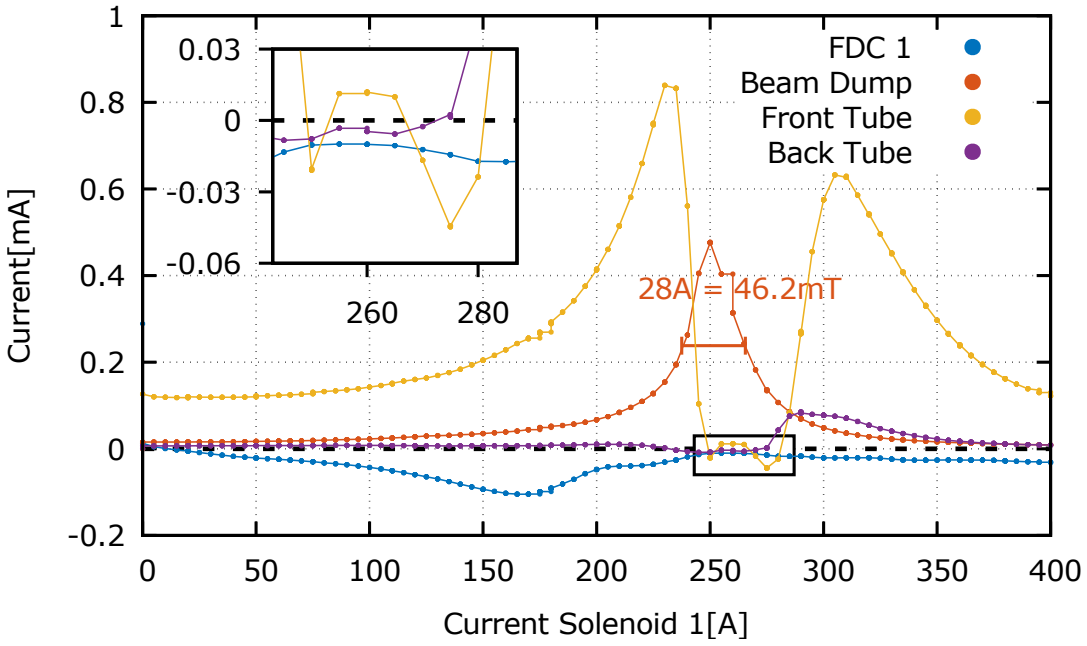

Figure 25: Solenoid 1 is varied with a He^+ beam energy at 50 keV. The full width half maximum (FWHM) value of the transmission is given. The measurement was done with setup 1 and FDC1 is moved out.

the magnetic field. Both explanations presume that the magnetic induction in the sub 165 mT regime is strong enough to influence the electrons, but too weak to influence the 50 keV Helium beam significantly, because a helium atom is more than 7000 times heavier than an electron.

Above 165 mT, the focusing of the solenoid dominates and the measured current increases up to a maximum. There is a yet unexplained step at 225 A which appears consistently in both measurement directions. In addition, a very slight hysteresis effect is visible between the measurement with decreasing and increasing current. An overly fast measurement speed should be eliminated as a cause for the hysteresis, because there is no offset in current at the start (0 A) or the end (400 A) between the measurements. The decreasing current above 340 A indicates that the solenoid begins to over-focus, which is in agreement with the expectation.

Fig. 25 shows the transmission through the beam line according to setup 1. All elements in the beam line were grounded if not otherwise stated. The current on the chopper tube closest to the ion source (front tube, yellow line) has two distinct maxima surrounding the optimal transmission into the second Faraday cup (beam dump). The losses on the front tube are consistent with the measurements by Nowottnick [Nowottnick, 2014, p. 33]. The first maximum, which corresponds to an under-focused beam, seems to be higher than the second maximum, which corresponds to an over-focused beam. The impact angle (deviation from perpendicular impact) should be higher in the

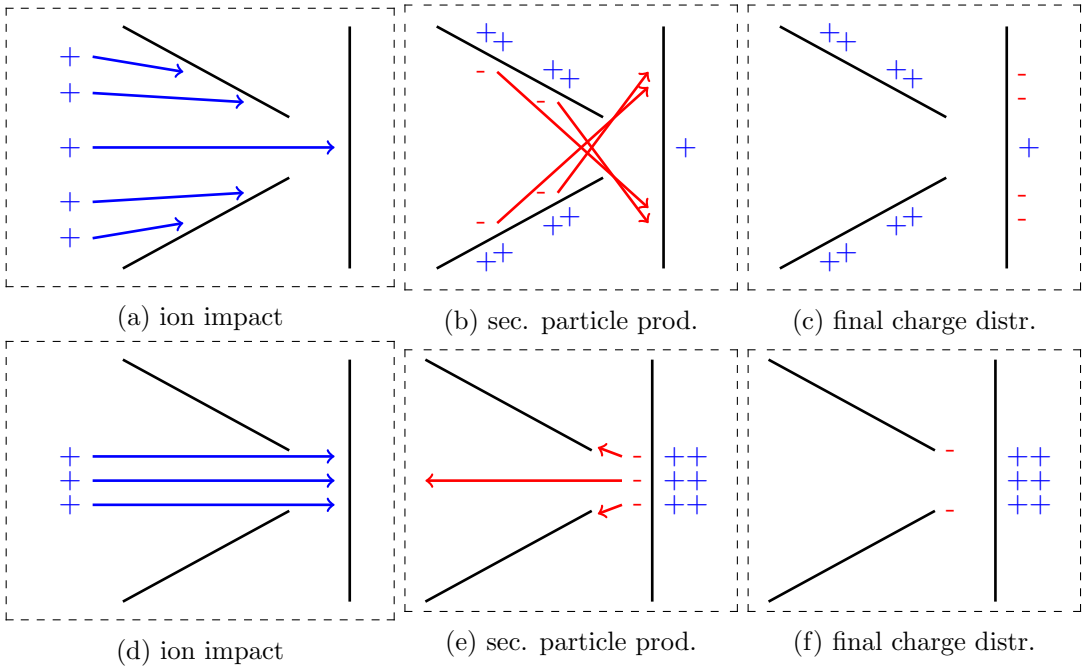

Figure 26: Two possible processes (a-c, d-f) of secondary particle production and their influence on measured currents is illustrated schematically. Positively charged ions are blue, negative secondary particles are red.

under-focused case compared to the over-focused case. A deviation in impact angle is a significant factor, because it is known to influence the secondary electron yield significantly [Svensson et al., 1981, p. 3751]. The magnified area shows the behaviour of the front tube current at and slightly after optimal transmission. The two dips in current below zero appeared consistently in measurements and seem to be characteristic. The first dip coincides with the maximum in transmission. It is followed by a plateau with positive current, which is followed by the second dip below zero. A possible interpretation is that the first dip is caused by secondary particles that were produced by the chopper plates and scattered back onto the tubes (similar effect in fig. 26 (d-f), for tube geometry see Fig. 5). The plateau might be caused by a reduction in backscattered secondary particles due to optimal transmission, in addition to halo particles directly impacting the tube. In addition, the current caused by the halo particles might be amplified by secondary particles (similar effect in fig. 26 (a-c)). The second dip might be the consequence of the slightly over-focused beam scrapping along the chopper tubes again. Similar to the case of the maxima, the current of the second dip is below the first one, which indicates a larger impact angle of the ions (less amplification). This interpretation is consistent with the geometry of the curved plates and the (amplified) current in the second tube (back tube) and appears in the measurement in Fig. 27 (a) as well. This effect will only be visible in simulations which include secondary particle emission from surfaces.

FDC 1 is supposed to be used as an emergency beam stopper and usually moved out of the beam line during experiments. The negative current is most likely caused by the secondary particles of a badly focused beam at the walls of the tubing. The full width half maximum (FWHM) of the transmitted current to the beam dump is 46.2 mT. With an effective solenoid field length of 324 mm and a distance of 3962 mm between solenoid 1 and beam dump an approximate particle radius can be obtained with the simple model from section 2.2.1. The resulting r_P/r_A ratio of about 2.5, assuming a precise particle energy of 50 keV corresponds to a particle radius of 125 mm, which is significant larger than the radius of solenoid 1. Assuming the beam is restricted by the round chopper plates (1364 mm from solenoid 1), the magnetic induction width of 46.2 mT results in a r_P/r_A of 4.5 and a particle radius of 86 mm, which is slightly more than the 75 mm radius of the solenoid. However, the simple model does not account for the space charge forces which might additionally defocus the beam during the more than 2.5 m drift after the chopper plates. An additional defocusing would cause an overestimation of the particle radius which would be consistent with the result, but needs validation.

All currents, except for FDC 1 and beam dump, might include secondary particle effects. Possible effects of secondary particles on the measured current are shown schematically in Fig. 26 for the cone-flange combination of setup 2. Here, the cone and flange are not grounded for illustration purposes. Depending on the secondary particle production rate, the measured currents might be off by up to a factor of 2 if the ions impact perpendicular to the surface (comp. [Lin and Joy, 2005, p. 898]). If the impact angle deviates only slightly from 0° (perpendicular to surface), the secondary electron yield might increase up to 10 and beyond [Svensson et al., 1981, p. 3751]. In case the effect of fig. 26 (d-f) is dominant, the secondary electrons function like an amplifier for the current on the flange. In the situation depicted in fig. 26 (a-c), the current on the flange is suppressed according to the amplification of the current on the cone. Due to the canonical shape of the cone it, should predominately either recapture secondary particles or transport them to be collected by the flange behind it. As a result, the combined currents of flange and cone should be reasonably close to the true value. However, the production process in fig. 26 (d-f) shows that backscattering might introduce losses which cannot be accounted for.

The transmission through the beam line according to setup 2 is shown in Fig. 27. In Fig. 27 (a), only the first solenoid is used to focus the beam. Complete transmission seems to be almost non-existent. In contrast to setup 1, the final aperture of the cone is significantly smaller (5 mm compared to 50 mm in radius). Geometrically, the combination of the cone and the flange are about the size of the Faraday cup in setup 1. Both secondary particle production processes described before seem to have no major effect. The current on the flange shows no amplification or drop below zero and the current on the cone is not significantly amplified or suppressed compared to the measurement in setup 1. For a single solenoid the 10 mm wide final aperture of the cone seems to be simply too small to achieve significant transmission.

The deviation between the current measured on the cone and the combination of cone and flange is very small in Fig. 27 (a). The deviation becomes pronounced when

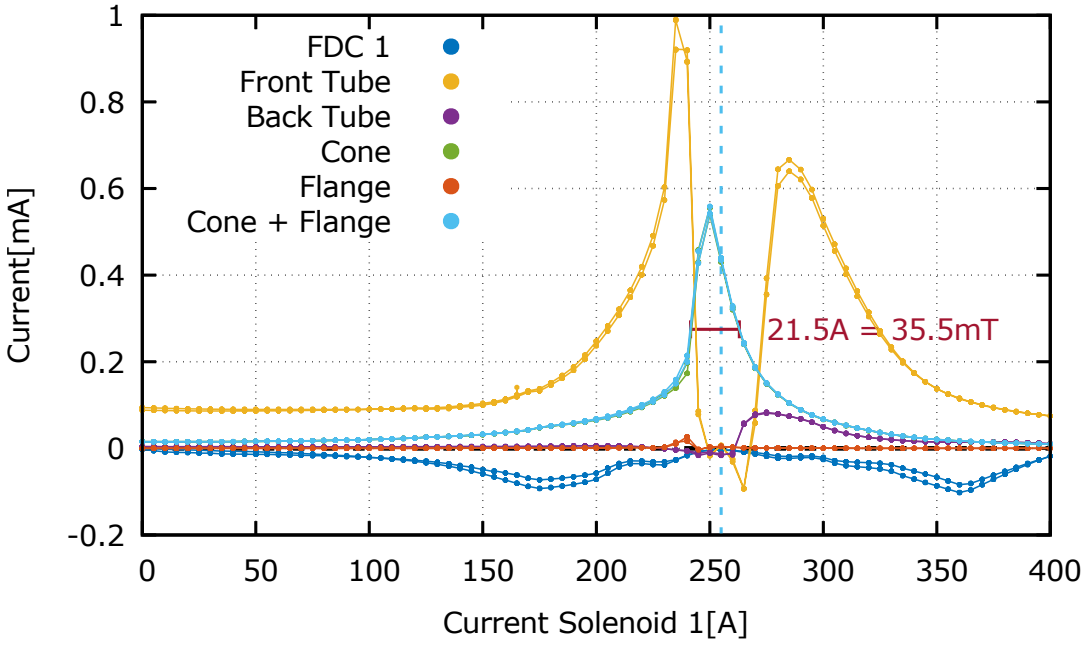

(a) Transmission in dependence of solenoid 1.

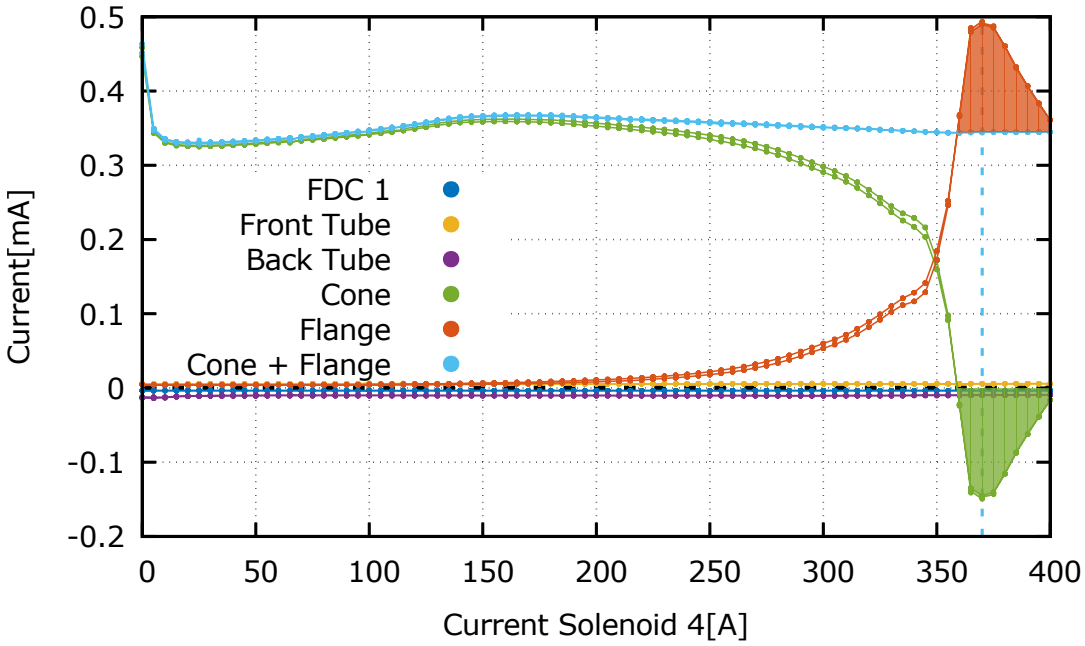

(b) Transmission in dependence of solenoid 4. Solenoid 1 is configured according to the light blue dashed line in (a).

Figure 27: Transmission of a 50 keV He^+ beam with about 1 mA current. The beam line is prepared according to setup 2.

the fourth solenoid is used (comp. Fig. 27 (b)). Once solenoid 4 focuses the beam so that it passes through the 10 mm aperture in the cone, the current on the flange rises, while it drops on the cone. The redistribution of the current between cone and flange happens while the combined current stays mostly constant (comp. light blue line). Most likely due to secondary particles produced on the flange which backscatter onto the back of the cone, the measured current on the cone drops below zero (comp. green area). Simultaneously, the current on the flange (comp. red area) is amplified accordingly. This observation is in good agreement with the effect described in fig. 26 (d-f).

Optimal transmission is assumed to be achieved at maximum current. At this point, most ions should pass the cone, impact on the flange and be amplified by secondary electrons. Secondary electron production rates depend, among others, on the initial particle energy, as well as the impact angle. The particle energy is supposed to be constant and the impact angle is assumed to vary slowly in comparison with the variation in solenoid strength. In this case, the amplification is linear, which does not alter the position of the current maximum. In any case, current shapes which include secondary particle effects should be interpreted very carefully.

In Fig. 27 (a), the FWHM of the solenoids magnetic induction is drawn. The width of 35.5 mT corresponds, according to the simple model from section 2.2.1, to a r_P/r_A ratio of about 3.5, assuming a precise particle energy of 50 keV and distance of 3557 mm between the flange and solenoid 1. The corresponding particle radius would be 175 mm, which is obviously incorrect. Assuming the beam is restricted by the chopper plates, the magnetic induction width of 35.5 mT results in a r_P/r_A of 6 and a particle radius of 114 mm, which still more than the 75 mm radius of solenoid 1.

The comparison of the simple model with the measurements yields that the calculations overestimate the particle radius about 14 % and 52 % compared to the maximum physically plausible value. The deviations could be caused by unconsidered repulsive forces (i.e. space charge) or are a result of other assumptions in the model (i.e. effective fields, linear optics, ...). A priori, it is not possible to decide if an error of 52 % is acceptable given the assumptions or not. Nevertheless, the huge increase in error between the setups is curious, because besides an about 500 mm shorter beam line with a different ion measurement method nothing has been changed. However, the results of the experiments agree with the intuitive expectation and the models prediction that the chopper plates are more limiting than the last aperture of solenoid 4. In addition, the combined cone-flange current in Fig 27 (b) suggests that solenoid 4 has little influence on the total current which can be measured behind it.

4.1.2 Variation in Beam Energy

The currents achieved while varying the beam energy are shown in Fig. 28. The focusing was adjusted according to the settings described in section 4.1.1. Although the extracted current increases with higher extraction voltage, the currents have not been corrected. Hence, the FWHM values might be slightly overestimated for theoretical comparisons, but are exact for the actual operation of the machine. Nevertheless, the offset between the maximum flange current and the combined maximum by 2 kV is independent of current corrections.

The simple model allows to calculate estimates which assume that solenoid 4 is off. With the geometric properties of the beam line and assumptions described in table (1) (a), the expected energy width of the transported current on the flange ΔE is 13.8 keV. In case a particle on the maximum inner radius of the solenoid is considered, the expected energy width on the flange shrinks to 6.8 keV. If the maximum instead of the minimum aperture of the cone is considered, the energy window becomes a bottom energy limit of 20.3 keV below reference. Based on the measurements in section 4.1.1, it is reasonable to check if the gap between the chopper plates could have an influence as well. If the chopper plates are assumed to be the limiting aperture, a particle on the maximum inner radius of the solenoid has an expected energy width of 27.8 keV. If a particle is at half of the radius, its energy has only a lower energy limit of 17.4 keV below reference. As a result, the model suggests that the chopper plates are still a limiting factor, but their significance vanishes compared to the small aperture of the cone.

The filter effect in Fig. 28 is characterized by the full width half maximum (FWHM) of the peak in measured current. The difference in width between the FWHM of the flange and the combined flange-cone current is 800 V. This small deviation is an indication that solenoid 4 actually matches most of the current through the cone onto the flange. The expected energy and momentum widths based on the simple model presented in section 2.2.1 are plotted in Fig. 29. The total expected energy width (yellow dashed line) is 13.8 keV for a matching onto the flange without solenoid 4. Either doubling the assumed radius of the cone r_A from 5 mm to 10 mm or halving the assumed particle radius r_P result in the values marked by the purple dashed line. Another halving or doubling is represented by the green dashed lines.

The FWHM values are 7 kV for the flange and 7.8 kV for the combination respectively, which corresponds to 14 % and 15.6 % of the total beam energy. The simple theoretical model predicts a sharp edge width of about 28 % for particles with an initial 37.5 mm beam axis offset. A total energy width of 14 % and 15.6 % correspond to a r_P/r_A of 13.5 and 14.5, which is equal to a particle radius of 67.5 mm and 72.5 mm. These radii are physically still possible, because the radius of the first solenoid is 75 mm.

The simple model is used for this two-solenoid-case, although it is only applicable for a single solenoid, because solenoid 4 seems to match the remaining beam without significant losses or gains into the cone (comp. Fig. 27) independent of its strength. Hence, solenoid 4 could be treated as part of the cone. The aperture of solenoid 4 is equal to the maximum aperture of the cone. But the estimations above predict only a bottom energy limit of 20.3 keV below reference for such a case, which does not fit the

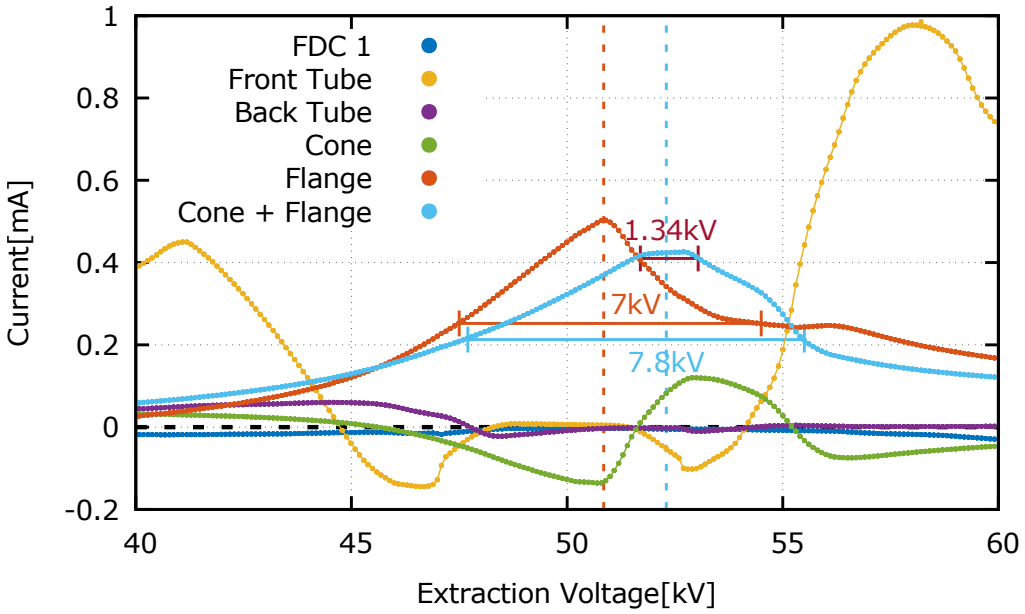

(a) Complete measurement

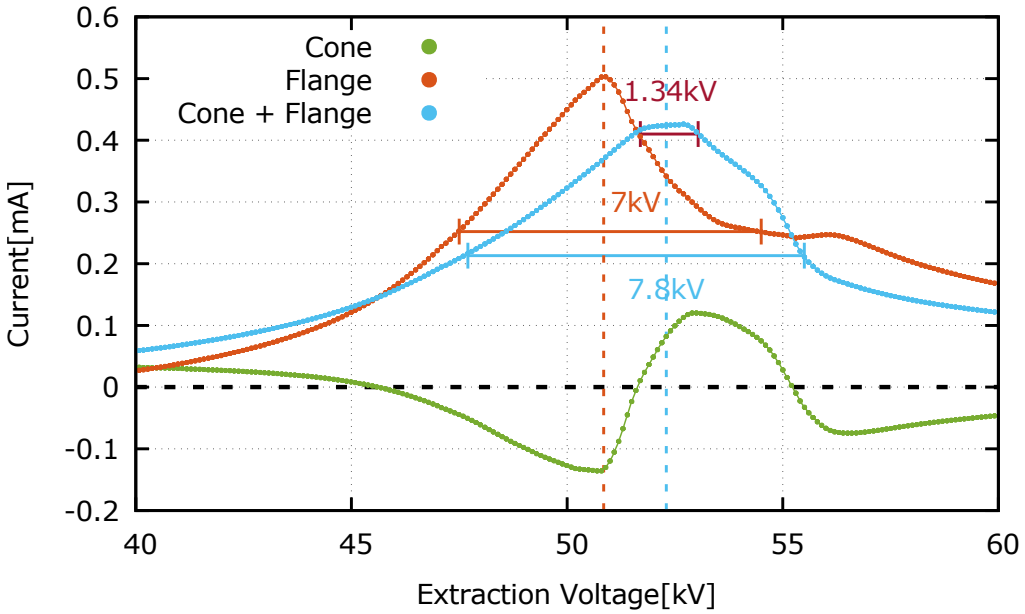

(b) Simplified version of (a) with relevant currents only.

Figure 28: The solenoids 1 and 4 are set to fixed values according to figure (27) (light blue dashed lines).

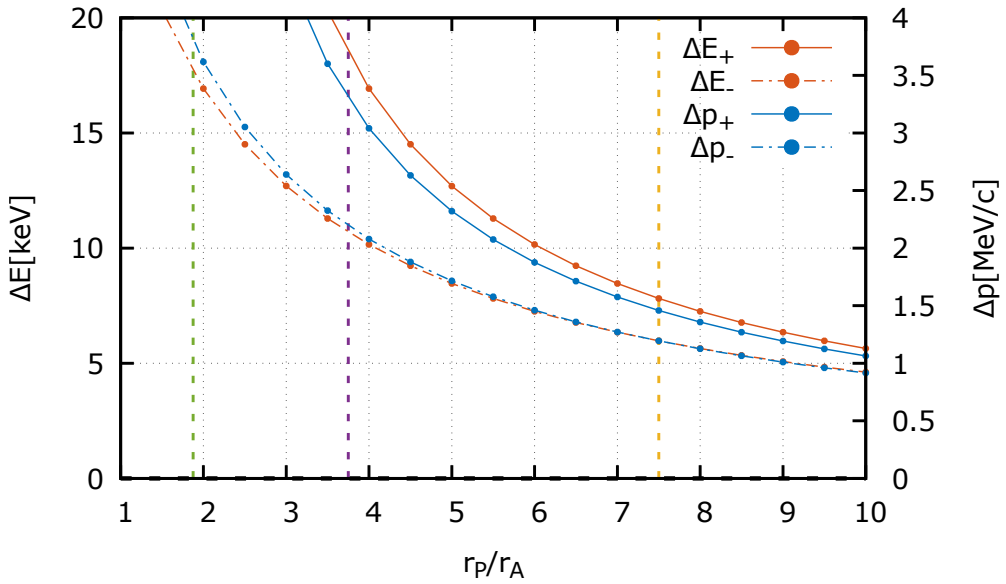

Figure 29: Numerical estimation of energy and momentum widths for LEBT setup 2 without small k approximation. The ratio r_P/r_A for a particle at half (yellow), one quarter (purple) and one eighth (green) of the solenoid radius is marked with dashed lines.

experiment. Strangely, the estimations which ignore solenoid 4 and assume a matching through the minimum aperture of the cone predict the FWHM values quite well. After all, the model cannot be validated and should not be applied for energy predictions yet. The limitations mentioned in section 4.1.1 most likely apply.

Besides testing the simple model in a real world scenario the measurements on the filtering by the solenoids and the apertures are the upper limit for the energy and momentum windows. Above all, the measurements are supposed to be a baseline for the following dipole and Wien filter measurements.

4.2 Dipoles

It is possible to use the dipoles in the chopper independently as a deflector. For the following measurements, the beam energy is kept at 50 keV. The electrostatic deflector applies positive voltage only. Bidirectional deflection is achieved by pole change and negative voltages imply that the pole has been changed. In order to compare the deflection via the electric and magnetic field, the current of the magnetic coil and the voltage of the electrostatic deflector are converted to an equivalent deflection force. At 6 kV, the effective field of the electromagnetic deflector is 314 kV/m [Wiesner, 2014, p. 45]. In standard operation mode, the electric dipole is operated at 4.7 kV and the corresponding maximum magnetic induction is 68.7 mT [Wiesner, 2014, p. 97, 103]. The force of the electric deflection is calculated via linear scaling:

$$F_{\text{elec}} = qE = q \cdot 314 \cdot \frac{U_{\text{exp}}}{6} \tag{69}$$

With U_{exp} being the actual voltage applied. The corresponding magnetic force is calculated using the knowledge that the forces are supposed to be equal, if the deflection voltage is 4.7 kV and the magnetic current is 68.7 mT. The formula for the magnetic force is:

$$F_{\text{mag}} = q \cdot 314000 \cdot \frac{4.7}{6} \cdot \frac{I_{\text{exp}}}{68.7} \tag{70}$$

With I_{exp} being the experimentally used current for the magnetic deflection. The results of the deflection measurements are shown in Fig. 30. In (a), the raw data is plotted. There is a significant difference in current between the flange and the combined flange cone current. The combination of the currents has a greater effect on the measurements with the magnetic dipole, which suggests that the significantly higher flange current is caused by secondary particle amplification (comp. Fig. 26). With the equations derived in section 2.2.2, it is possible to calculate an approximate deflection angle as well as the transversal offset behind the deflection plates. The distance between the end of the chopper plates and the beginning of the cone is 1898 mm. With an average FWHM of 12.4 fN, the sufficient force to deflect most of the beam is assumed to be 6.4 fN. The corresponding deflection voltage is 763 V. With eq. (41) and (42), the deflection angle at the end of the chopper and the offset at the beginning of the cone can be calculated. The deflection angle α is 55 mrad. Given the distance $d = 1.898$ mm between the chopper and the beginning of the cone, the total deflection is $s_x = 108$ mm.

The result of the deflection distance is slightly too large to fit the diameter of the cone opening, which is 100 mm, but still in a reasonable regime. The theoretical deflection voltage for a 100 mm offset is 704 V. The dipoles act like a fast-particle-pass filter. All particles below a critical threshold determined by the aperture are filtered. However, the passing particles might have gained significant transversal momentum. With Eq. (41), the measured 760 V FWHM corresponds to a theoretical critical limit of about 54 keV. Ions with an energy below 54 keV are not able to hit the cone, which is consistent with the deflection distance of 108 mm for 50 keV Ions.

A remaining curiosity is that the width of the dipole deflections is very similar for the cone and the flange, although they differ significantly in diameter. According to Fig.

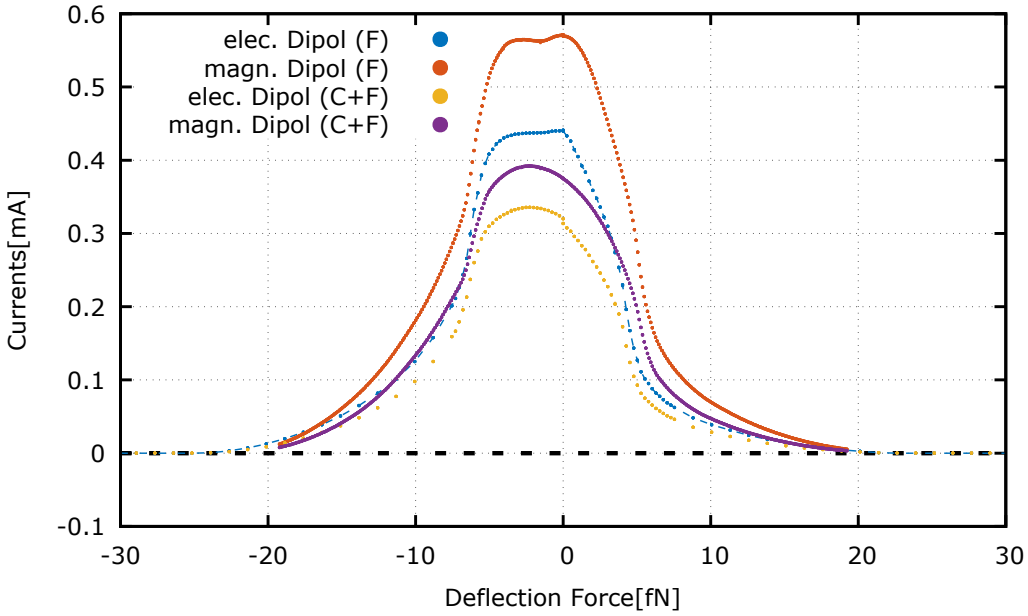

(a) without normalized current

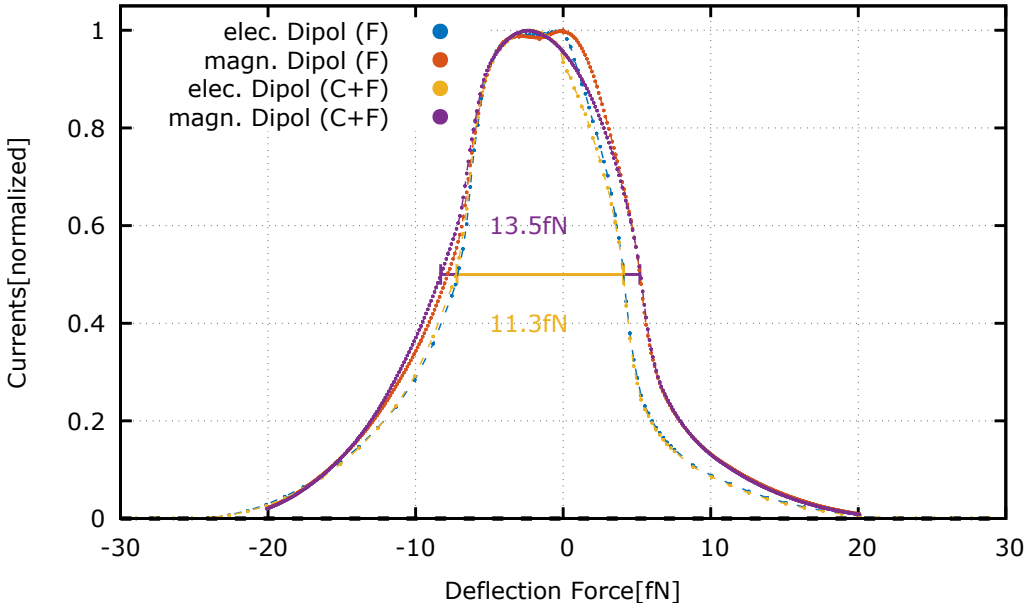

(b) with normalized current

Figure 30: Chopper deflection measurements with electric and magnetic dipoles. The energy of the He^+ beam is 50 keV at about 1 mA current and the beam line was configured according to setup 2. The currents on the flange (F) and the combined cone and flange currents (C+F) are shown. In (b), the full width half maxima are drawn.

(27), solenoid 4 is tuned to match the beam through the cone. If solenoid 4 matches the beam perfectly though the cone, the current on the flange corresponds to the current which enters solenoid 4. As a result, the measurements of the flange and the combined flange cone currents would be identical. Furthermore, in a non perfect case, the beam could be reflected by the surface of the cone onto the flange. The determination of such a reflection cross section should be subject to further research. The distance between the chopper section and the entrance of solenoid 4 is 1647 mm. Solenoid 4 has a diameter of 100 mm. A recalculation with these parameters yield a total deflection of 95 mm and a critical limit of 47.3 keV. The estimation above suggest that solenoid 4 maps most of the current directly onto the flange, which explains the similar FWHMs for the flange and the combined currents.

The expected shape of the drop in current while deflecting can be estimated via the area of two intersecting circles with radius r and R and the distance d between the radii[2].

$$\begin{aligned} A(R,r,d) =& r^2 \cdot \arccos\left(\frac{d^2+r^2-R^2}{2\cdot d\cdot r}\right) + R^2 \cdot \arccos\left(\frac{d^2+R^2-r^2}{2\cdot d\cdot R}\right) \\ & - \frac{1}{2}\cdot\sqrt{(-d+r+R)\cdot(d+r-R)\cdot(d-r+R)\cdot(d+r+R)} \end{aligned} \tag{71}$$

In Fig. 31, a fitted versions of Eq. (71) with additional scaling parameters are drawn with the electric dipole measurements. In general, the distribution of the measurement has a significantly longer tail, which is expected for a realistic distribution without sharp edges. The gradients of the upper slopes are in good agreement. As a result, the distribution is expected to be quite homogeneous in its core. The ratio of the fitted radii of the intersecting circles varies from 1.315 ± 0.005 for the right slope to 1.331 ± 0.003 for the left slope when combined currents are considered. For the flange only case, the ratios are 1.308 ± 0.006 for the right and 1.335 ± 0.005 for the left slope.

A cone or solenoid 4 radius of 50mm and a radii ratio of 1.32 corresponds to a beam radius of 38mm or 66mm, depending on whether the beam is assumed to be the smaller or larger one of the intersecting circles. The measurements in section 4.1.1, especially Fig. 27 (b), suggest that the beam is smaller than the aperture.

An attempt to find the actual origin of the distributions is shown in Fig. 32. In (a), the data is plotted dependent on the originally measured units. In (b), the ratio between the flange current and the combined flange and cone current is calculated. In line with the amplification hypothesis by secondary particles, the ratio is called amplification factor. The centred minimum is used as a reference point in order to determine the origin. The axis are scaled using the remaining extrema. As a result, 1 A deflection current is equal to 57.5 V of deflection voltage. The offset in deflection current is 3.7 A, the offset in deflection voltage is 230 V.

With magnetic deflection, the amplification factor is generally at least 10 % higher that with the electrical deflection. An apparent difference between magnetic and electric deflection is that the magnetic deflection force depends on the velocity of the particles, while the electric deflection force is constant for any particle of equal charge. In a

[2] http://mathworld.wolfram.com/Circle-CircleIntersection.html (20.01.2017)

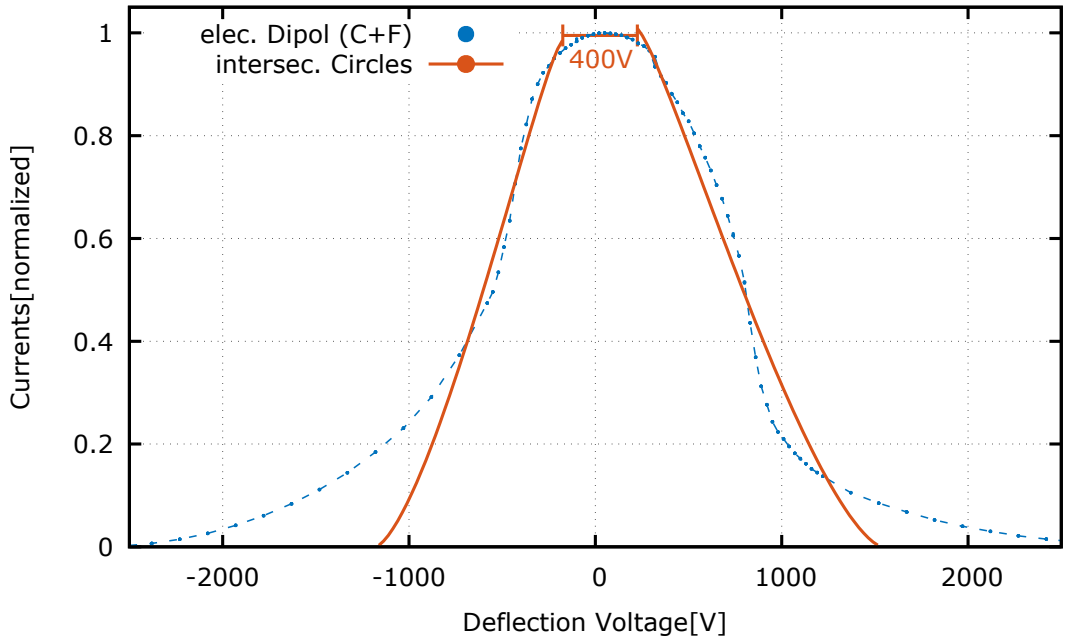

(a) Cone + Flange Currents

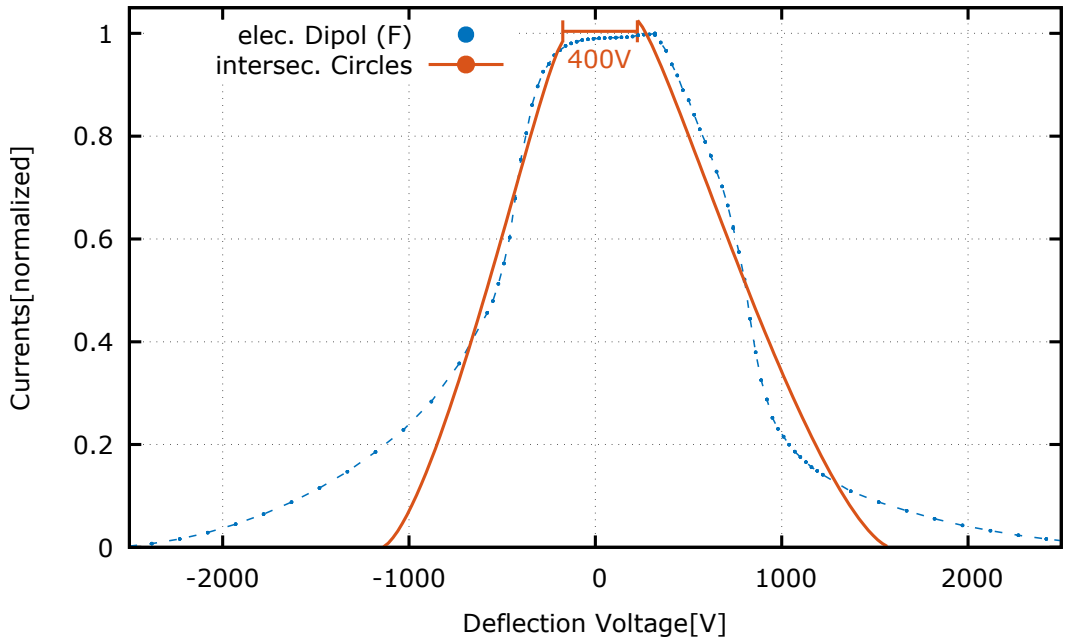

(b) Flange Current

Figure 31: Electric dipole measurements with original units, but moved to be centred around the origin. The function in Eq. (71) is fitted to the right and left slope separately.

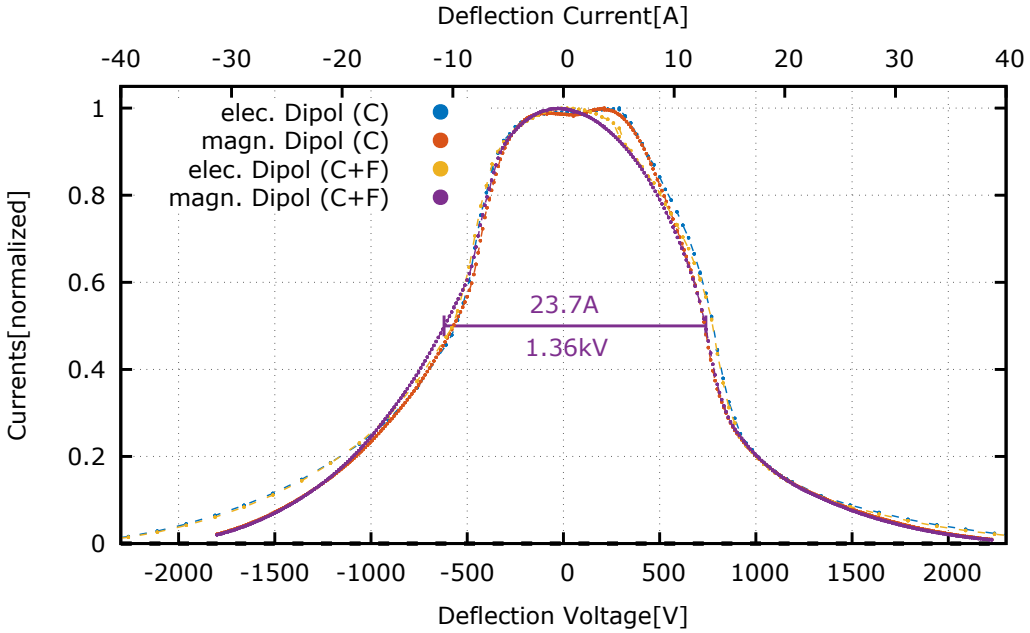

(a) Magnetic and electric dipole measurements with original units. 1 A magnetic current is equal to 57.5 V electric current. The data was recentred in order to be symmetrical to the origin.

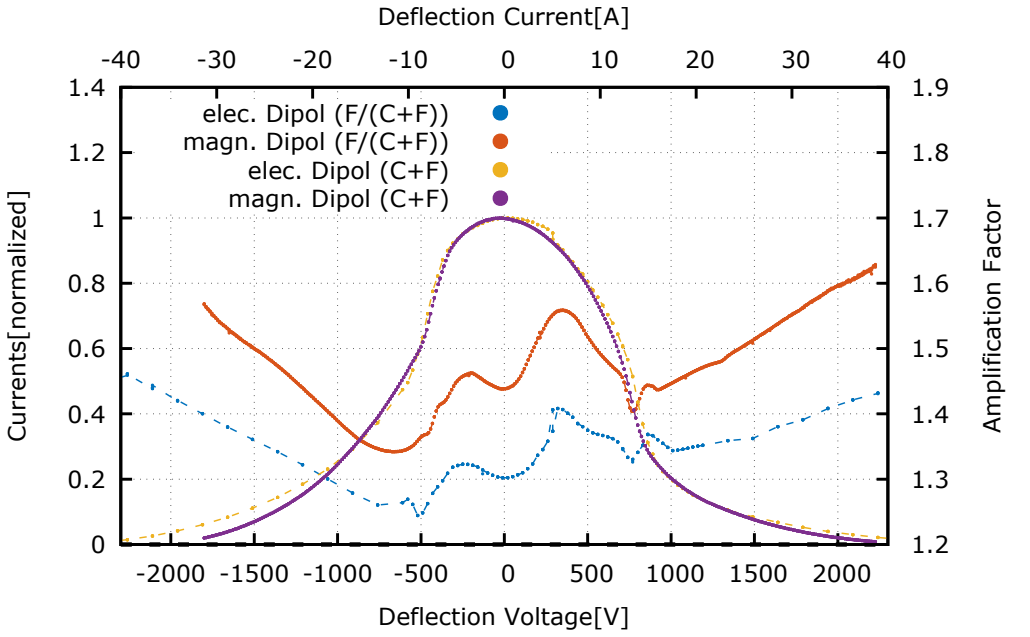

(b) Current and current amplification factor as a function of deflection voltage and current.

Figure 32: In (a), the measurement used before is presented with the actually measured units. In (b), the amplification factor between the flange and the combined flange cone current is calculated.

positively charged ion beam, electrons which are produced by collisions with the residual gas or by ion impacts with the tubing are transported as well. These electrons, being about 7400 times lighter than a helium ion, are filtered rigorously by the electrical field. However, if the electron is much slower than the helium ion, it should be less affected by the magnetic field than the ion. It can easily be calculated that electrons with a kinetic energy below 126 neV are able to pass the magnetic field. However, 126 neV is an unrealistically small energy for electrons.

A remaining difference between electric and magnetic deflection is an electrical field transports electrons to the positive pole, whereas the magnetic field mostly confines them at the magnetic sheath. With Eq. (45), the cyclotron radius of a slow 1 eV electron in a 1 mT magnetic field is 3 mm, which is a worst-case scenario. Usually, the magnetic field is about a magnitude higher and the electrons are most likely faster. Depending on their transversal momentum, the electrons will gyrate towards the magnetic poles. The gyration should happen slowly compared to the deflection of the electric field. Hence, an explanation for the over all difference between electric and magnetic deflection could be that an electrical field removes the electrons from the beam, whereas a magnetic field only separates the two section downstream and upstream of the chopper in terms of electrons in the beam. With more electrons being in the magnetically deflected beam, more electrons can impact the flange and create more secondary electrons, thus amplifying the current similar to impacting ions. The maximum secondary electron yield for electrons impacting on copper is $\delta_m = 1.56$ (comp. [Lin and Joy, 2005, p. 898]), which appears ad hoc reasonable in order to explain the difference in currents. An unexpected asymmetrical skewness is noticeable in the slope independent of the dipole type. With the shifted maxima the asymmetrical skewness is another indication for a slight misalignment of the beam.

4.3 Wien Configuration

In addition to the single use of each dipole independently, they can also be used in simultaneous operation as a Wien filter. As shown in section 2.2.4, the Wien filter is sensitive to the particles' velocity. In this section, measurements done at the end of the experimental cycle are shown.

All following measurements are done with a Wien condition designed for a He^+ beam at 40 keV. The refraction power of the solenoids is kept constant (comp. Fig. 16) in order to suppress the filter effect of the solenoids. Eq. (64) states that the deflection depends on the electrical field, the acceleration voltage and the deviation factor. As a result, the relative filter effect on 40 keV He^+ should be equal to the design 120 keV H^+ beam. The electrical field is achieved using positive high voltage.

Fig. 33 (a) shows the measured current without the Wien filter being active. Solenoids 1 and 4 were used to focus the beam. The negative current on the cone is consistent with the measurements in section 4.1. In contrast, the Wien filter was active in Fig. 33 (b). The Wien condition was experimentally determined. At 40 keV, maximum transmission was achieved, with 4.5 kV voltage between the deflection plates and a magnetic induction of 73 mT. The filter effect is stronger for particles that are too slow compared to particles that are too fast. This behaviour is a direct consequence of the inversely proportional dependency of the deflection distance on the acceleration voltage of the particle. According to Eq. (64), a particle which is 20 % slower than 40 keV (32 keV) is deflected by 10.5 mm at the entrance of the chopper, whereas a particle which is 20 % faster (48 keV) is only deflected by 6.4 mm. The difference of about a factor of 2 is roughly consistent with the measurement (see norm(F+C)). Besides the general shape, the influence of the data acquisition and processing is shown via the different currents for the flange and the cone. Measurements marked with "norm" have been normalized using the reference measurement. From the non-normalized current on the flange to the normalized combined current on flange and cone, the filter effect supposedly "improves" while the maximum moves towards its expected position. This result is in contrast to the measurement shown in section 4.1.2 Fig. 28, where the combined flange cone current is further away from its expected position.

Finally, Fig. 34 shows a comparison between the measurement with the collimation channel and the Wien filter. Although the measurements have been performed around different design energies, there are distinct differences. The filter effect of the collimation channel remains relevant for faster-than-reference particles, whereas the Wien filter flattens significantly. Furthermore, the top of the maxima is wider in the Wien filter case. However, the influence of the Wien filter on the particle is independent of the particle position compared to the collimation channel.

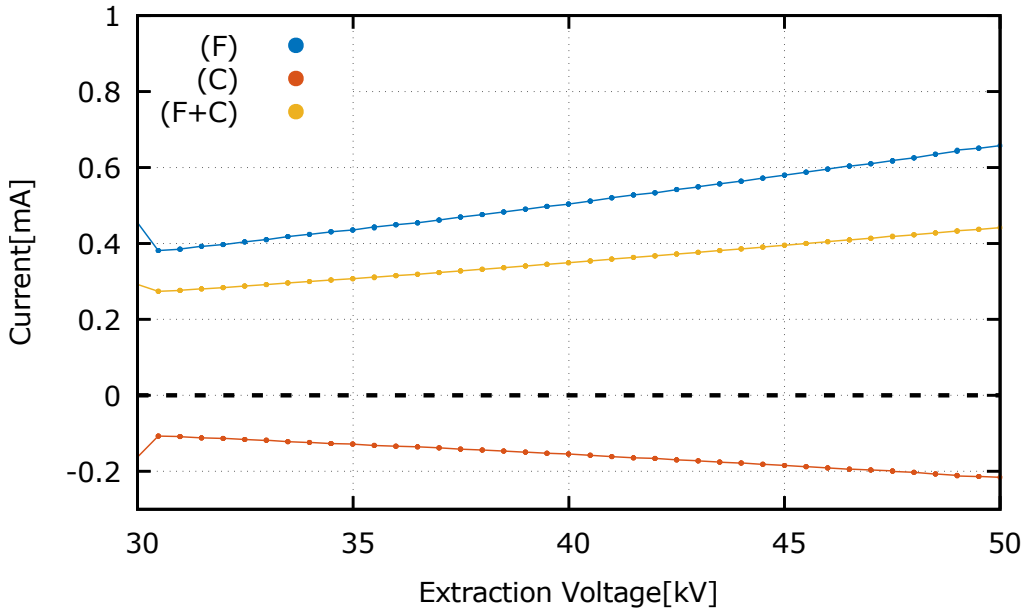

(a) reference measurement

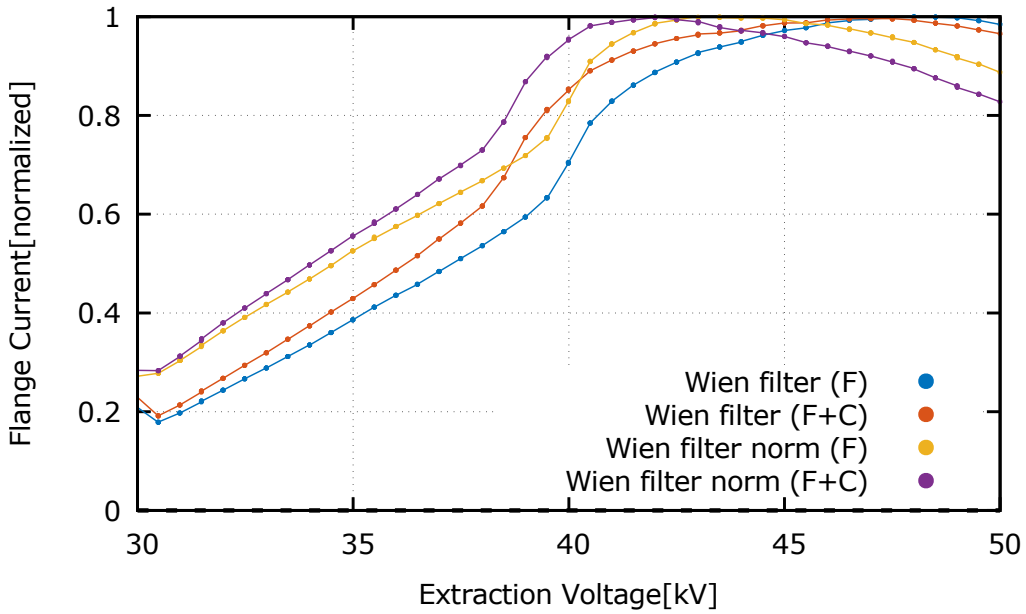

(b) normalized transmission

Figure 33: In (a), reference transmission measurements with deactivated Wien filter are shown. They are used in order to normalize the measurements in (b). The dipoles in the Wien filter are set to 4.7 kV and 73 A. The measurements denoted with "norm" are normalized using the measurement in (a).

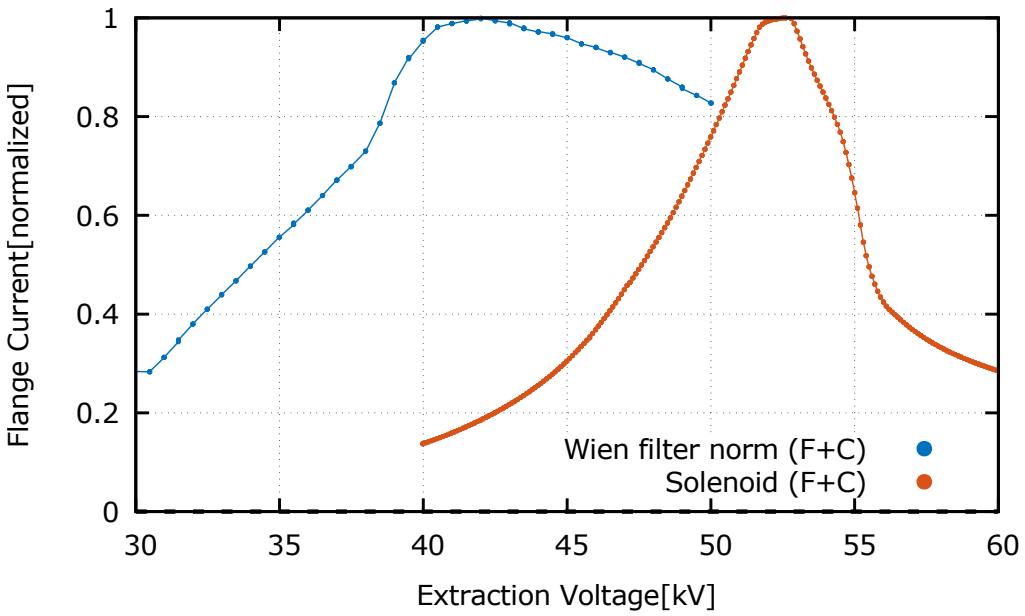

Figure 34: The measurement from section 4.1.2 is compared to the Wien filter measurement. The design value for the solenoid filter is 50 keV and the design value for the Wien filter is 40 keV.

5 Conclusion

In this thesis, a script for MNDACS was developed in order to enable automatic and repeatable measurements while manipulating various power supplies simultaneously. During the conditioning phase of the extraction system, multiple measurements were recorded, which show a dependency between a rise in pressure and a rise in extraction voltage. Degassings which coincided with a voltage increase contributed to at least 5 % and up to 25 % of the total number of events depending on the degassing strength, while degassings which coincided with voltage drops contributed to less than 2.5 % of the events. In order to improve the significance of the coincidence between voltage rises and degassings, controlled long-term measurements with no effective increase in voltage (square wave-like shape) are proposed. Additional parameters of interest could be different total voltage levels as well as different amplitude values for the voltage wave. It is not yet determined which voltage steps are able to provide the most or the strongest degassing events. Additionally, the production of controlled degassing while avoiding total voltage breakdowns was found to be particularly difficult and has not yet been thoroughly explored. An ion source with insulators transparent to UV, visible light and IR (i.e. fused silica) might help understand the location, path, power and frequency of spark overs. In addition, IR spectrometers can monitor the heat distribution and thermal stress on the electrodes.

With a simple light beam based model, it was theoretically shown that halo particles from unwanted fractions can be filtered by the solenoids and the geometric properties of a beam line only (collimation channel). The filtering happens due to a difference in momentum. The strength of the filtering highly depends on the radial distance of the particle. The larger the radius, the greater the filter effect. Close to the beam axis, the filter effect vanishes. For particles with smaller-than-reference momentum, a filter effect remains even if the particle radius is smaller than the aperture it is supposed to pass ($r_P/r_A < 1$). For larger-than-reference momentum particles, there is no filter effect once the particles have a radius of about the size of the aperture.

An asymmetric filter effect was found experimentally for He^+ at 50 keV reference energy. The simple model could not be verified or falsified during the measurements. However, the asymmetry was in agreement with the theoretical prediction. The deflection measurements were in reasonable agreement with the theoretical predictions based on effective fields. By calculating the area of two intersecting circles with different radii, an ad hoc ansatz was introduced which might be capable of estimating the width of an ion beam. Refining the method by using the intersection of a density distribution and a circle might lead to more accurate results. If a dipole is already part of a beam line, this intersecting method might be a simple possibility to obtain rough beam radii estimates for low power beams. In case the dipoles are used in Wien configuration, they are able to filter ions as well. Assuming that the particles have been accelerated by a static electrical field, the filter is sensitive to the ratio of charge to mass. Classically, a Wien filter acts as a velocity selector. On its own, the Wien filter performed weaker in comparison to the collimation channel. However, the Wien filter is able to select the particles inde-

pendently of their position in the beam. As a result, the Wien filter should be able to compensate the drawbacks of a collimation channel when used in series. Lastly, analysis on the secondary particle effects on the current of the cone-flange-construction according to setup 2 were done. Given the assumption presented with respect to secondary particle production, the current on the flange was amplified by a factor of up to 1.6. The amplification had a significant offset between the electric and the magnetic dipole. The magnetic dipole had a consistent and significantly higher amplification factor than the electrical dipole. Additional electrons which are removed by the electrical dipole, but are only reflected or confined by the magnetic dipole, might cause this significant and consistent difference by impacting on the flange and producing their own secondary particles.

In conclusion, a collimation channel is likely to filter unwanted ion fractions from a beam's halo and outer shell, especially with a Wien filter upstream. Dipoles might be usable in order to determine an estimate beam radius. Degassings rates in extraction systems were increased by at least 10 % via variations in voltage.

6 Appendix

6.1 Source code of MNDACS Script

In this section, only the functional parts of the MNDACS script are presented. The code is highly experimental and still uses global variables extensively. Due to its proof-of-principle character, it is not recommended to use this script for daily work, yet. This excerpt is supposed to be used as a reference point for further improvements or debugging. The AutomodeMulti class is supposed to be initialized as a thread.

```
/**
* List of global variables used:
* dev_ properties define the properties of the three PSUs:
* - currentvalue = current value which is supposed to be set
* - start = start value
* - step = stepsize for increments or decrements
* - end = end value
*
* t_ramp and t_mes are global properties for all PSUs
* which define the duration of the pauses between steps
* (t_ramp) and between measurements at a certain step (t_meas).
*
* part_q and part_b define the ion charge state in multiples
* of e and the mass of the ion in multiples of u
*
* kvalues stores the refraktive power for the four solenoids
*
* automode_valperstep defines how many measurements are done
* at each step
*
* dev_totsteps stores the total amount of steps for a run
*
* automode_currentstep stores the current step number
*/
double dev_currentvalue, dev_start, dev_step , dev_end;
double dev_currentvalue1, dev_start1, dev_step1 , dev_end1;
double dev_currentvalue2, dev_start2, dev_step2 , dev_end2;
double t_ramp, t_mes;
double part_q=0, part_m=0;
ArrayList<Double> kvalues = new ArrayList<Double>();
boolean PSU1_on, PSU2_on;
long automode_valpstep, dev_totsteps
, automode_currentstep = 0;
boolean automode_bidirect_sweep = false;
```

```
class AutomodeMulti extends SwingWorker<Void, Void>{
 /**
 * In order to make different rising modes work with
 * all PSUs at the same time, the AutomodeMulti
 * class has to be initialized for each PSU
 * independently.
 */

 private void updateSolenoids(){
 /**
 * Function which controls the solendoids in case
 * constant refraction power is enabled
 */
 double tempB=0, tempI=0, terminalvoltage=0;
 dal.doDriverFunction("PSU-LEBT-8", "getValues"
  , "null", null, null, null, null);
 ArrayList<ValueSet>values1
  = DAL.getReturnValueSet("PSU-LEBT-8");
 for (int i=0; i<values1.size(); i++){
  if(values1.get(i).info.equals("Voltage reference")){
   terminalvoltage = values1.get(i).DoubleValue;
  }
 }
 for(int i=1; i<5; i++){
  tempB = 2*kvalues.get(i-1)
   *Math.sqrt((2*part_m*terminalvoltage)/part_q)
   /Math.sqrt(95788340.96);
  tempI = tempB*1000/660*400;
  System.out.println("Sol"+i+"I: "+tempI);
  String device_name = "PSU-LEBT-"+i;
  dal.doDriverFunction(device_name, "setCurrent"
   , "double", null, null, tempI, null);
  }
 }

 private void setPSUValue(String dev_name
  , double dev_currentval, boolean voltagemode  ){
  /**
  * Sets the new value of a device via the dal object
  */
  if(voltagemode){
   dal.doDriverFunction(dev_name, "setVoltage"
    , "double", null, null, dev_currentval, null);
```

```
 }else{
  dal.doDriverFunction(dev_name, "setCurrent"
    , "double", null, null, dev_currentval, null);
 }
}

private boolean setVoltageMode(String dev_valname){
 /**
 * Determines if the voltage or the current is
 * supposed to be set.
 */
 if(dev_valname.contains("Current")){
  return false;
 }else if(dev_valname.contains("Voltage")){
  return true;
 }else{
  return true;
 }
}

private void updatePSUs(String dev_name
 , String dev_name1, String dev_name2, boolean voltmode
 , boolean voltmode1, boolean voltmode2){
 /**
 * Function which
 */
 setPSUValue(dev_name, dev_currentvalue, voltmode);
 if(PSU1_on){
  setPSUValue(dev_name1, dev_currentvalue1, voltmode1);
 }
 if(PSU2_on){
  setPSUValue(dev_name2, dev_currentvalue2, voltmode2);
 }
 if(cb_solenoidcontrol.isSelected()){
  updateSolenoids();
 }
}

@Override
protected void doInBackground() throws Exception {
 boolean voltagemode, voltagemode1 = true
  , voltagemode2 = true;
 StorageMulti measurements = null;
```

```
automode_currentstep = 0;
String device_name1 = null, device_name2 = null;
int item = cb_rising_modes.getSelectedIndex();

String device_name
 = (String) cb_devices_automode.getSelectedItem();
dev_currentvalue = dev_start;
voltagemode = setVoltageMode((String)
 cb_device_values_automode.getSelectedItem());

if(PSU1_on){
 device_name1 =(String)
  cb_devices_automode1.getSelectedItem();
 dev_currentvalue1 = dev_start1;
 voltagemode1 = setVoltageMode((String)
  cb_device_values_automode1.getSelectedItem());
}
if(PSU2_on){
 device_name2 =(String)
  cb_devices_automode2.getSelectedItem();
 dev_currentvalue2= dev_start2;
 voltagemode2 = setVoltageMode((String)
  cb_device_values_automode2.getSelectedItem());
}
// get inital value for measurement
updatePSUs(device_name, device_name1, device_name2
 , voltagemode, voltagemode1, voltagemode2);
Thread.sleep((long)(t_ramp*1000));
measurements = new StorageMulti();
measurements.execute();
Thread.sleep((long)(automode_valpstep*t_mes*1000));

// loop which sets device values
for(int i = 1;  i< dev_totsteps; i++){
 switch (item){
  //normal mode
  //up, down, up
  //up, down, up, wait
  default:dev_currentvalue = dev_currentvalue + dev_step;
   dev_currentvalue1 = dev_currentvalue1 + dev_step1;
   dev_currentvalue2 = dev_currentvalue2 + dev_step2;
  break;
  //small up, small up, down, up, wait
```

```
 case 3: dev_currentvalue = dev_currentvalue + (dev_step/2);
  dev_currentvalue1 = dev_currentvalue1 + dev_step1;
  dev_currentvalue2 = dev_currentvalue2 + dev_step2;
 break;
 }
updatePSUs(device_name, device_name1, device_name2
 , voltagemode, voltagemode1, voltagemode2);
updateTimeEstimate();
Thread.sleep((long)(t_ramp*1000));
measurements = new StorageMulti();
measurements.execute();


switch (item){
 //up, down, up
 case 1: Thread.sleep(
   (long)(automode_valpstep*t_mes*1000/2));
  dev_currentvalue = dev_currentvalue - dev_step;
  setPSUValue(device_name, dev_currentvalue, voltagemode);
  Thread.sleep((long)(automode_valpstep*t_mes*1000/2));
  dev_currentvalue = dev_currentvalue + dev_step;
  setPSUValue(device_name, dev_currentvalue, voltagemode);
 break;
 //up, down, up, wait
 case 2: Thread.sleep(
   (long)(automode_valpstep*t_mes*1000/3));
  dev_currentvalue = dev_currentvalue - dev_step;
  setPSUValue(device_name, dev_currentvalue, voltagemode);
  Thread.sleep((long)(automode_valpstep*t_mes*1000/3));
  dev_currentvalue = dev_currentvalue + dev_step;
  setPSUValue(device_name, dev_currentvalue, voltagemode);
  Thread.sleep((long)(automode_valpstep*t_mes*1000/3));
 break;
 //small up, small up, down, up, wait
  case 3: Thread.sleep(
    (long)(automode_valpstep*t_mes*1000/4));
  dev_currentvalue = dev_currentvalue + (dev_step/2);
  setPSUValue(device_name, dev_currentvalue, voltagemode);
  Thread.sleep((long)(automode_valpstep*t_mes*1000/4));
  dev_currentvalue = dev_currentvalue - dev_step;
  setPSUValue(device_name, dev_currentvalue, voltagemode);
  Thread.sleep((long)(automode_valpstep*t_mes*1000/4));
  dev_currentvalue = dev_currentvalue + dev_step;
```

```
 setPSUValue(device_name, dev_currentvalue, voltagemode);
 Thread.sleep((long)(automode_valpstep*t_mes*1000/4));
break;
//f. up, down, up, f. down, up, wait
case 4: Thread.sleep(
  (long)(automode_valpstep*t_mes*1000/8));
 dev_currentvalue = dev_currentvalue - dev_step;
 setPSUValue(device_name, dev_currentvalue, voltagemode);
 Thread.sleep((long)(automode_valpstep*t_mes*1000/4));
 dev_currentvalue = dev_currentvalue + dev_step;
 setPSUValue(device_name, dev_currentvalue, voltagemode);
 Thread.sleep((long)(automode_valpstep*t_mes*1000/4));
 dev_currentvalue = dev_currentvalue - dev_step;
 setPSUValue(device_name, dev_currentvalue, voltagemode);
 Thread.sleep((long)(automode_valpstep*t_mes*1000/8));
 dev_currentvalue = dev_currentvalue + dev_step;
 setPSUValue(device_name, dev_currentvalue, voltagemode);
 Thread.sleep((long)(automode_valpstep*t_mes*1000/4));
break;
//f. up, down, up, f. sm. down, f. up, f. sm. down, wait
case 5: Thread.sleep(
  (long)(automode_valpstep*t_mes*1000/8));
 //down
 dev_currentvalue = dev_currentvalue - dev_step;
 setPSUValue(device_name, dev_currentvalue, voltagemode);
 Thread.sleep((long)(automode_valpstep*t_mes*1000/4));
 //up
 dev_currentvalue = dev_currentvalue + dev_step;
 setPSUValue(device_name, dev_currentvalue, voltagemode);
 Thread.sleep((long)(automode_valpstep*t_mes*1000/4));
 //fast small down
 dev_currentvalue = dev_currentvalue - (dev_step/2);
 setPSUValue(device_name, dev_currentvalue, voltagemode);
 Thread.sleep((long)(automode_valpstep*t_mes*1000/8));
 //fast up
 dev_currentvalue = dev_currentvalue + dev_step;
 setPSUValue(device_name, dev_currentvalue, voltagemode);
 Thread.sleep((long)(automode_valpstep*t_mes*1000/8));
 //fast small down
 dev_currentvalue = dev_currentvalue - (dev_step/2);
 setPSUValue(device_name, dev_currentvalue, voltagemode);
 Thread.sleep((long)(automode_valpstep*t_mes*1000/8));
break;
```

```
   default:Thread.sleep((long)(automode_valpstep*t_mes*1000));
   break;
  }
this.setProgress((int)((double)
 automode_currentstep/(dev_totsteps*automode_valpstep)*100));
}
```

```
if(automode_bidirect_sweep){
 automode_currentstep = 0;
 dev_currentvalue = dev_currentvalue + dev_step;
 dev_currentvalue1 = dev_currentvalue1 + dev_step1;
 dev_currentvalue2 = dev_currentvalue2 + dev_step2;
 for(int k = 0;  k< dev_totsteps; k++){
  dev_currentvalue = dev_currentvalue - dev_step;
  dev_currentvalue1 = dev_currentvalue1 - dev_step1;
  dev_currentvalue2 = dev_currentvalue2 - dev_step2;
  updateTimeEstimate();
  //System.out.println(dev_currentvalue);
  setPSUValue(device_name, dev_currentvalue, voltagemode);

  if(PSU1_on){
   setPSUValue(device_name1
    , dev_currentvalue1, voltagemode1);
  }


  if(PSU2_on){
   setPSUValue(device_name2
    , dev_currentvalue2, voltagemode2);
  }


  if(cb_solenoidcontrol.isSelected()){
   updateSolenoids();
  }
  Thread.sleep((long)(t_ramp*1000));

  measurements = new StorageMulti();
  measurements.execute();
```

```
      Thread.sleep((long)(automode_valpstep*t_mes*1000));

     }
    }



 return null;
 }

@Override
 protected void done(){
 this.setProgress(0);
 b_save.setEnabled(true);
 b_open.setEnabled(true);
 tf_start.setEnabled(true);
 tf_stepsize.setEnabled(true);
 tf_end.setEnabled(true);
 tf_rampdelay.setEnabled(true);
 tf_stepdelay.setEnabled(true);
 tf_valuespstep.setEnabled(true);
 b_automode_start.setEnabled(true);
 b_automode_stop.setEnabled(false);
 tb_automode_status.setBackground(Color.red);
 tb_automode_status.setText("stoped");
 automode_currentstep = 0;
 tf_q.setEnabled(true);
 tf_m.setEnabled(true);
 cb_rising_edge.setEnabled(true);
 cb_rising_modes.setEnabled(true);
 updateTimeEstimate();
 }
} // End of class AutomodeMulti

class StorageMulti extends SwingWorker<Void, Void>{

 @Override
 protected Void doInBackground() throws Exception {
  for(int l = 1; l <= automode_valpstep; l++){
   automode_currentstep++;

   updateAndSafeAutomode();
```

```
    Thread.sleep((long)(t_mes*1000));
   }
  return null;
  }

  @Override
  protected void done(){
  }
}// End of class StorageMulti

/*
*Action Event which invokes the AutomodeMulti object
*/

private void b_automode_startActionPerformed
 (java.awt.event.ActionEvent evt) {
 // Some modifications to the UI
 b_save.setEnabled(false);
 b_open.setEnabled(false);
 tf_start.setEnabled(false);
 tf_stepsize.setEnabled(false);
 tf_end.setEnabled(false);
 tf_rampdelay.setEnabled(false);
 tf_stepdelay.setEnabled(false);
 tf_valuespstep.setEnabled(false);
 cb_rising_edge.setEnabled(false);
 cb_rising_modes.setEnabled(false);
 b_automode_start.setEnabled(false);
 b_automode_stop.setEnabled(true);

 //set solenoid refraction powers
 if(cb_solenoidcontrol.isSelected()){
  tf_q.setEnabled(false);
  tf_m.setEnabled(false);
  double tempcurrent=0, tempfield, tempvoltage=1, tempk;
  part_q = Double.parseDouble(tf_q.getText());
  part_m = Double.parseDouble(tf_m.getText());
  dal.doDriverFunction("PSU-LEBT-8", "getValues"
   , "null", null, null, null, null);
  ArrayList<ValueSet>values1 = DAL.getReturnValueSet
   ("PSU-LEBT-8");
  for (int i=0; i<values1.size(); i++){
   if(values1.get(i).info.equals("Voltage_reference")){
```

```
    tempvoltage = values1.get(i).DoubleValue;
   }
  }


  for(int j=1; j < 5; j++){
   if (kvalues.size()<j){
    kvalues.add(0.0);
   }
   String devicename = "PSU-LEBT-"+j;
   dal.doDriverFunction(devicename, "getValues"
    , "null", null, null, null, null);
   ArrayList<ValueSet>values
    = DAL.getReturnValueSet(devicename);
   for (int i=0; i<values.size(); i++){
    if(values.get(i).info.equals("Current reference")){
     tempcurrent = values.get(i).DoubleValue;
    }
   }
   tempfield = tempcurrent/400*660/1000;
   tempk = Math.sqrt(95788340.96)*(tempfield/2)
    *Math.sqrt(part_q/(2*part_m*tempvoltage));
   kvalues.set(j-1, tempk);
   switch (j){
    case 1: l_k1.setText("k_1 = "+String.format("%.3f",tempk));
   break;
    case 2: l_k2.setText("k_2 = "+String.format("%.3f",tempk));
   break;
    case 3: l_k3.setText("k_3 = "+String.format("%.3f",tempk));
   break;
    case 4: l_k4.setText("k_4 = "+String.format("%.3f",tempk));
   break;
    default: break;
   }
  }
}
/*
* Initialize and start run. Property change listener is used
* for progress bar
*/
instance = new AutomodeMulti();
instance.addPropertyChangeListener(
 new PropertyChangeListener() {
```

```
    @Override
    public void propertyChange(PropertyChangeEvent evt) {
     if ("progress".equals(evt.getPropertyName())) {
      pb_automode.setValue((Integer)evt.getNewValue());
     }
     pb_automode.setString(automode_currentstep+"/"
      +dev_totsteps*automode_valpstep);
    }
   }
  );
  instance.execute();
  tb_automode_status.setBackground(Color.green);
  tb_automode_status.setText("running");
}
```

Acknowledgements

I thank:

Prof. Dr. Holger Podlech for the support of and the opportunity to do my Master's Thesis in accelerator physics.

The NNP group for the sincere and warm welcome as well as the provision of such a great and motivating working environment.

Christoph Wiesner for his kind and detail-oriented supervision throughout all circumstances.

Oliver Meusel for his seemingly infinite amount of possible research directions, problem solutions and motivation. I am especially thankful for the pure glimpse at the operational and administrative procedures in research at IAP.

Daniel Noll for the introduction to his simulation codes and thorough support with inconsistently occurring computer or network issues.

Philipp "Fips" Schneider for his handy tips and tricks for surviving every day life in experimental physics.

Christopher Wagner for providing and introducing me to the MNDACS control system and his support concerning question about electrical engineering.

Thomas Metz for his almost instantly and always available support and service in at manual works and technical constructions.

The IKF precision engineering workshop for their straightforward and precise realization of unconventional and untimely machining tasks.

My fiancée and family for their loving and unconditional support as well as some critical questions which helped me to focus during the different phases of this thesis.

Christoph Beberweil and Thomas Kelly for softening the linguistic edges of my English.

Last but not least, I would like to thank everyone which I unintentionally forgot to mention in this section. My gratitude might not be recorded on this paper but in my heart.

List of Figures

List of Tables

Bibliography

S. Alzubaidi, U. Bartz, M. Basten, A. Bechtold, L. P. Chau, C. Claessens, H. Dinter, M. Droba, C. Fix, H. Hähnel, et al. The Frankfurt neutron source FRANZ. *The European Physical Journal Plus*, 131(5):1–13, 2016.

L. Arnaudon, M. Magistris, M. Paoluzzi, M. Hori, D. Küchler, P. Bourquin, K. Hanke, R. Wegner, C. Rossi, G. Bellodi, et al. Linac4 technical design report. Technical report, 2006.

K. Bosch. Gesetze der großen Zahlen. In *Elementare Einführung in die Wahrscheinlichkeitsrechnung*. Springer, Jan. 2011. ISBN 978-3-8348-1861-4. doi: 10.1007/978-3-8348-8331-5_3. URL `http://dx.doi.org/10.1007/978-3-8348-8331-5_3`.

J. D. Cockcroft and E. T. S. Walton. Experiments with high velocity positive ions. (i) further developments in the method of obtaining high velocity positive ions. *Proceedings of the Royal Society of London. Series A, Containing Papers of a Mathematical and Physical Character*, 136(830):pp. 619–630, 1932. ISSN 09501207. URL `http://www.jstor.org/stable/95811`.

L. Dahl, W. Barth, and S. Yaramishev. Transport and injection of heavy ion beams with high brilliance for the GSI high current injector. In *XXI International Linac Conference, 19th-23rd August*, 2002.

M. Heilmann, D. Mäder, O. Meusel, U. Ratzinger, A. Schempp, and M. Schwarz. A coupled RFQ-IH cavity for the neutron source FRANZ. *Proceedings of IPAC2013, Shanghai, China, THPWO017*, page 3797, 2013.

F. Hinterberger. *Physik der Teilchenbeschleuniger und Ionenoptik*. Springer-Verlag, 2008.

C. Lefevre. The CERN accelerator complex. Technical report, CERN, 2008.

Y. Lin and D. C. Joy. A new examination of secondary electron yield data. *Surface and Interface analysis*, 37(11):895–900, 2005.

A. Lombardi. Commisioning of the low energy part of the low-energy part of LINAC4. Talk at LINAC 14, 2014.

M. Lotz. Fokussier- und Abbildungseigenschaften von Solenoiden. Master's thesis, Johann Wolfgang Goethe-Universität, 2011.

D. J. MacKay. *Information theory, inference, and learning algorithms*, volume 7. Citeseer, 2003.

D. Marić, M. Savić, J. Sivoš, N. Škoro, M. Radmilović-Radjenović, G. Malović, and Z. L. Petrović. Gas breakdown and secondary electron yields. *The European Physical Journal D*, 68(6):1–7, 2014.

O. Meusel, L. Chau, M. Heilmann, H. Podlech, U. Ratzinger, K. Volk, C. Wiesner, et al. FRANZ–accelerator test bench and neutron source. *MO3A03, LINAC*, 12, 2012.

T. Nowottnick. Strahltransportsimulationen und -experimente durch einen Solenoidkanal. Master's thesis, Johann Wolfgang Goethe-Universität, 2014.

S. Peggs, R. Kreier, C. Carlile, R. Miyamoto, A. Pahlsson, M. Trojer, and J. Weisend II. ESS technical design report. *European Spallation Source ESS AB*, 2013.

J. Pfister, O. Meusel, O. Kester, et al. Collimation of high intensity ion beams. *Proceedings of IPAC2011, San Sebastián, Spain IPAC*, pages 2403–2405, 2011.

J. Pozimski. Messungen an einer Gabor-Plasma-Linse. 1990.

M. Reiser. *Theory and design of charged particle beams*. John Wiley & Sons, 1994.

L. Sachs and J. Hedderich. *Angewandte Statistik*. Springer Verlag, Berlin, New, 2008.

A. Schempp et al. Overview of recent RFQ projects. In *Proceeding LINAC*, 2008.

R. Schmidt, J. Jeanneret, J. Wenninger, B. Dehning, V. Kain, H. Burkhardt, B. Puccio, B. Goddard, R. Assmann, and E. Carlier. Beam loss scenarios and strategies for machine protection at the LHC. In *AIP Conf. Proc.*, volume 693, pages 184–187, 2003.

R. Schmidt, R. Assmann, E. Carlier, B. Dehning, R. Denz, B. Goddard, E. Holzer, V. Kain, B. Puccio, B. Todd, et al. Protection of the CERN large hadron collider. *New Journal of Physics*, 8(11):290, 2006.

S. Schmidt. *Neutrons at FRANZ: production and data acquisition systems*. PhD thesis, Johann Wolfgang Goethe-Universität, 2015. URL `http://exp-astro.physik.uni-frankfurt.de/docs/schmidt_15_phd.pdf`.

P. P. Schneider. Anpassung von Ionenstrahlen an die Akzeptanz eines RFQ. Master's thesis, Johann Wolfgang Goethe-Universität, 2014.

W. Schweizer, U. Ratzinger, B. Klump, and K. Volk. A high intensity 200 mA proton source for the FRANZ-project (Frankfurt-Neutron-Source at the Stern-Gerlach-Center). *Review of Scientific Instruments*, 85(2):02A743, 2014.

B. Svensson, G. Holmen, and A. Buren. Angular dependence of the ion-induced secondary-electron yield from solids. *Physical Review B*, 24(7):3749, 1981.

W. Umrath, R. Bahnen, and K. L. V. GmbH. *Grundlagen der Vakuumtechnik*. Leybold Vakuum, 1997.

R. J. Van De Graaff. A 1,500,000 volt electrostatic generator. *Phys. Rev*, 38:1919, 1931.

C. Wagner. Optische tomographische Strahldiagnose. Master's thesis, Johann Wolfgang Goethe-Universität, 2013.

H. Wiedemann. *Particle accelerator physics*. Springer Science & Business Media, 2007.

C. Wiesner. Schnelles Choppersystem für hochintensive Ionenstrahlen. Master's thesis, Johann Wolfgang Goethe-Universität, 2008.

C. Wiesner. *Chopping and transport of high-intensity ion beams*. PhD thesis, Johann Wolfgang Goethe-Universität, 2014.

C. Wiesner, H. Dinter, M. Droba, O. Meusel, D. Noll, T. Nowottnick, O. Payir, U. Ratzinger, and P. Schneider. Experimental performance of an E×B chopper system. *Proceedings of IPAC*, 2014.

C. Wiesner, S. Alzubaidi, M. Droba, M. Heilmann, O. Hinrichs, B. Klump, O. Meusel, D. Noll, O. Payir, H. Podlech, et al. FRANZ and small-scale accelerator-driven neutron sources. 2015.

C. Zhang, H. Klein, D. Mäder, H. Podlech, U. Ratzinger, A. Schempp, R. Tiede, and M. Vossberg. Front-end linac design and beam dynamics simulations for MYRRHA. In *Proceedings of the LINAC12 Conference, Tel Aviv*, pages 849–851, 2012.

Erklärung

Erklärung nach § 30 (12) Ordnung für den Bachelor- und dem Masterstudiengang:

Hiermit erkläre ich, dass ich die Arbeit selbstständig und ohne Benutzung anderer als der angegebenen Quellen und Hilfsmittel verfasst habe. Alle Stellen der Arbeit, die wörtlich oder sinngemäß aus Veröffentlichungen oder aus anderen fremden Texten entnommen wurden, sind von mir als solche kenntlich gemacht worden. Ferner erkläre ich, dass die Arbeit nicht - auch nicht auszugsweise - für eine andere Prüfung verwendet wurde.

Frankfurt, den